Front. Optoelectron. 2014, 7(2): 199–219
DOI 10.1007/s12200-014-0397-3

RESEARCH ARTICLE

Toward remote sensing with broadband terahertz waves

Benjamin CLOUGH[1], Xi-Cheng ZHANG (✉)[2,3]

1 Rensselaer Polytechnic Institute, Troy, NY 12180-3590, USA
2 The Institute of Optics, University of Rochester, Rochester, NY 14627-0186, USA
3 Wuhan National Laboratory for Optoelectronics, Huazhong University of Science and Technology, Wuhan 430074, China

Abstract This paper studies laser air-photonics used for remote sensing of short pulses of electromagnetic radiation at terahertz frequency. Through the laser ionization process, the air is capable of generating terahertz field strengths greater than 1 MV/cm, useful bandwidths over 100 terahertz, and highly directional emission patterns. Following ionization and plasma formation, the emitted plasma acoustic or fluorescence can be modulated by an external terahertz field to serve as omnidirectional, broadband, electromagnetic sensor. These results help to close the "terahertz gap" once existing between electronic and optical frequencies, and the acoustic and fluorescence detection methodologies developed provide promising new avenues for extending the useful range of terahertz wave technology. Our experimental results indicate that by hearing the sound or seeing the fluorescence, coherent detection of broadband terahertz wave at remote distance is feasible.

Keywords terahertz, air, plasma, fluorescence, acoustic

1 Introduction

Terahertz electromagnetic waves, defined as the frequency region between 0.1 and 10 terahertz on the electromagnetic spectrum, have demonstrated remarkable usefulness for imaging and chemical identification with the ability to penetrate many optically opaque barriers. Photon energies at these frequencies are relatively small (meV), which means the radiation is non-ionizing and therefore considered biologically innocuous. With the growing list of applications and demand for terahertz technology, there is a need to develop innovative terahertz sources and detectors that can overcome existing limitations in power, bandwidth, and operating range. Although terahertz radiation has demonstrated unique and exceptional abilities, it has also presented several fundamental challenges. Most notably, the water vapor absorption of terahertz waves in air at habitable altitudes is greater than 100 dB/km. There is an immediate push to utilize the material and vapor identification abilities of terahertz radiation, while extending the effective distances over which the technology can be used. Remote terahertz detection, until recently, was thought to be impossible due to the high water content in the atmosphere, limited signal collection geometries, and solid state materials necessary for generation and detection.

Received December 9, 2013; accepted January 21, 2014

E-mail: xi-cheng.zhang@rochester.edu

2 Terahertz air photonics

Terahertz wave generation from intense laser-plasma interaction in air was first reported by Hamster et al. in 1993 [1]. At the time, single color (800 nm) subpicosecond laser pulses were used, and the generation process was attributed to the ponderomotive force inside the plasma. In 2000, Cook and Hochstrasser reported that higher intensity terahertz radiation could be emitted from laser-induced gas-plasma excited with both a fundamental pulse (800 nm) and its second harmonic (400 nm) [2]. The terahertz wave emission mechanism was attributed to the four-wave mixing (FWM) nonlinear optical process. At that time, several other groups became interested in this topic. Among them, Bartel et al. reported terahertz wave generation from gas-plasma with peak electric fields higher than 100 kV/cm, indicating promising applications of the gas-plasma terahertz wave source [3]. However, the physical process for terahertz wave emission remained under debate. In order to identify the basic mechanism, coherent control experiments were performed which verified that FWM could be used to explain the terahertz wave generation process in a gas-plasma [4]. More importantly, using the FWM approximation, the detection of broadband pulsed terahertz waves with a laser-induced

gas-plasma was successfully predicted and experimentally demonstrated [5].

2.1 Generation and detection of terahertz waves in air

Terahertz air photonic systems differentiate themselves from other terahertz time-domain spectrometers by using ambient air or selected gases for the generation and detection of broadband pulsed terahertz waves [4–7]. Figure 1(a) illustrates the schematic diagram for a terahertz air biased coherent detection (THz-ABCD) spectroscopic system in both transmission and reflection mode. Figure 1 (b) illustrates plasma formed after focusing a high-energy laser pulse into the air.

A Ti:Sapphire regenerative amplifier is typically used as the laser source. Such a laser delivers laser pulses with millijoule pulse energy, femtosecond pulse duration, 800 nm center wavelength, and kilohertz repetition rate. The beam is split into pump and probe beams using a beamsplitter. The pump beam is focused through a beta-barium borate (β-BBO) crystal to produce the second harmonic at 400 nm. The mixed fundamental and second harmonic beams (ω and 2ω respectively) generate the ionizing plasma spot (center-right of Fig. 1(b)) that emits intense, directional, and ultra-broadband terahertz radiation through a third-order nonlinear process [2]. Although FWM cannot completely describe the complex physical details [8–11], it remains a convenient framework for experimental results due to its simplicity. After interaction with a sample, the remaining terahertz energy and optical probe beam are recombined at the detection region, where an electric bias (E_{bias}) is applied to create a second harmonic local oscillator for coherent detection through DC-field-induced second harmonic generation [12]. Figure 2 shows that the terahertz field is proportional to the intensity of the fundamental pulse (ω) above the ionization threshold for lower intensities, and is proportional to the square root of the second harmonic pulse (2ω) [13]:

$$E_{\text{THz}} \propto \chi^{(3)} \sqrt{I_{2\omega}} I_{\omega}. \quad (1)$$

It is important to note that this relationship is only valid for relatively low peak laser power intensities, since FWM is an approximation invalid when the intensity is high. At higher laser power intensities, the plasma electron density increases and reduces the Debye length. In other words, there is a screening effect that no longer yields a linear relationship between the THz amplitude and the peak laser power.

Similar to the widely used generation and detection of terahertz waves in electro-optic crystals by second order optical nonlinearity [14–16], terahertz waves can be detected by the third order optical nonlinearity in air or other selected gases [5,6]. Figures 3(a) and 3(b) plot terahertz waveforms and spectra detected with laser-induced air-plasma using THz-ABCD in comparison with the conventional electro-optic method with an electro-optic ZnTe crystal as the sensor. Using air as the sensor, the spectrum from 0.3 to over 30 terahertz sufficiently covers the "terahertz gap". Using shorter laser pulses, terahertz peak fields may exceed 1 MV/cm, and the spectrum may extend beyond 120 terahertz [17]. As a comparison, the DC breakdown threshold for air is about 30 kV/cm.

The use of air to sense pulsed terahertz waves is a measurement of the terahertz field induced optical second harmonic light generated through a third-order nonlinear process that has been investigated extensively in the previous literature [12,18,19], and therefore details will not be presented here. The measured second harmonic intensity can be expressed as

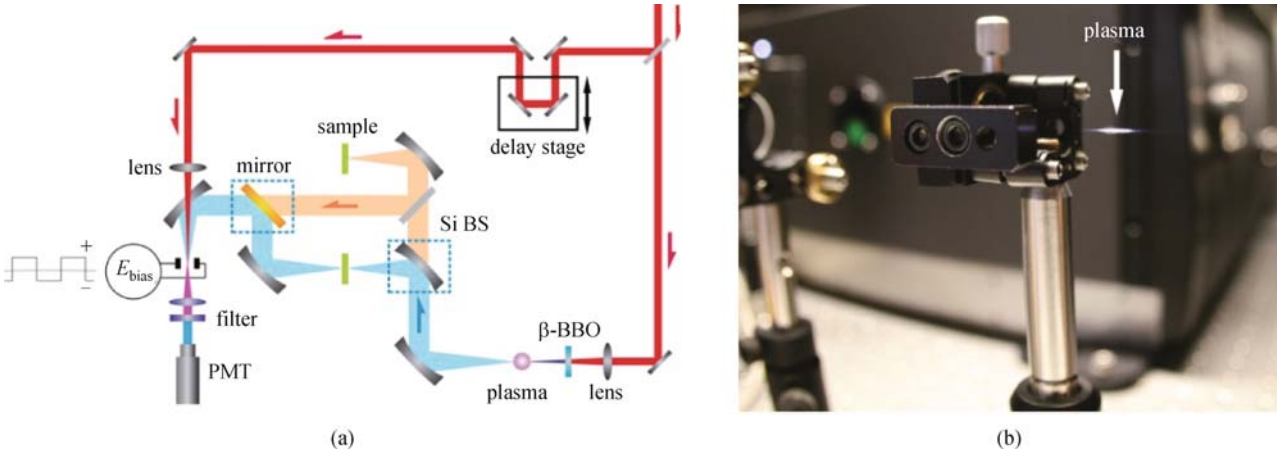

Fig. 1 (a) Schematic diagram of a THz-ABCD spectroscopic system in both transmission and reflection mode. The system can be converted from transmission to reflection mode by taking out the mirrors indicated with an enclosing dashed box. PMT: photomultiplier tube; BS: beamsplitter; β-BBO: beta-barium borate; (b) photograph of laser-induced air-plasma created after focusing the optical beam from left to right through a lens (left) and mounted nonlinear crystal (center) used for second harmonic generation. The bright horizontal line emits an intense, highly directional terahertz field to the right

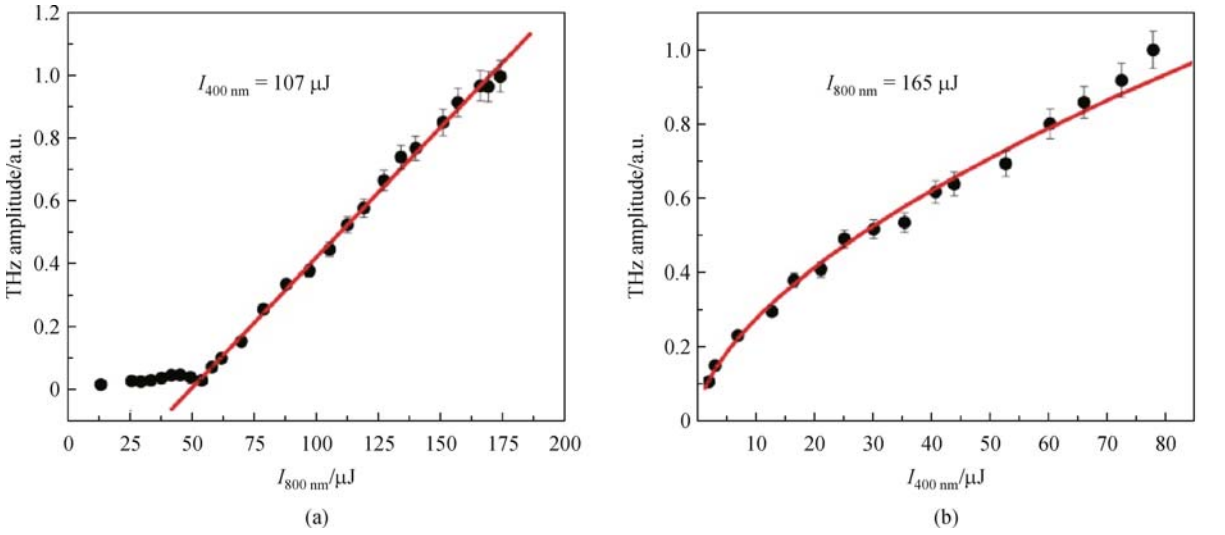

Fig. 2 (a) Dependence of terahertz field on fundamental (ω) pulse energy, with fixed second-harmonic (2ω) pulse energy; (b) dependence of terahertz field on second-harmonic pulse energy, with fixed fundamental pulse energy. The solid line and curve are the linear and square-root fits, respectively. Reprinted figure with permission from Ref. [4]

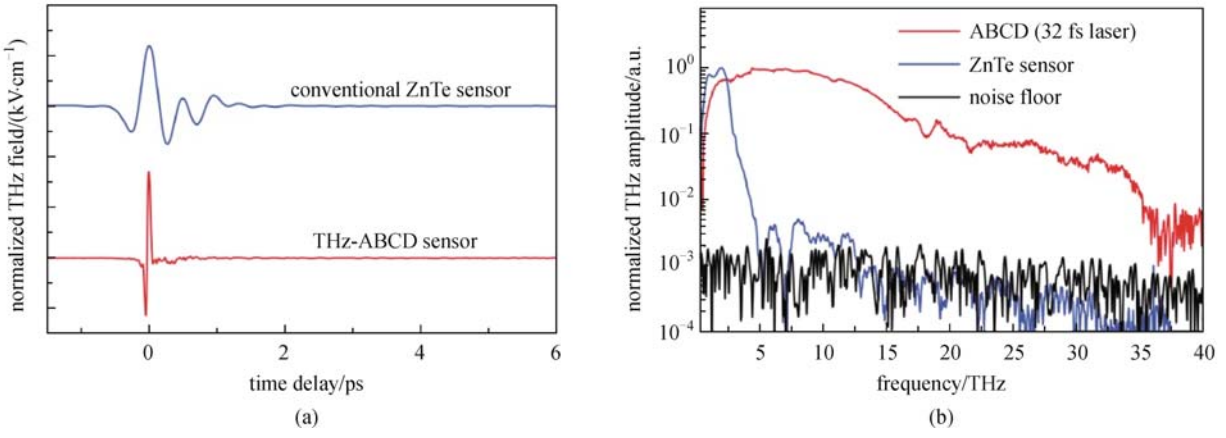

Fig. 3 (a) Time-resolved terahertz signals generated and detected using dry nitrogen gas as compared to conventional electro-optic (EO) crystal detection in ZnTe. The probe beam for air detection has energy of 85 μJ and pulse duration of 32 fs; (b) corresponding spectra after Fourier transformation

$$I_{2\omega}(\tau) \propto 2[\chi^{(3)} I_{\omega}(t)]^2 E_{\text{bias}} E_{\text{THz}}(t-\tau). \quad (2)$$

Equation (2) is the key description for detection. The linear dependence of $I_{2\omega}$ on E_{bias} indicates heterodyne detection when E_{bias} is treated as a local oscillator. The field-induced second harmonic signal $I_{2\omega}$ is quadratically proportional to $\chi^{(3)}$ and $I_{\omega}(t)$, and linearly proportional to E_{bias} and $E_{\text{THz}}(t-\tau)$.

Figure 4(a) illustrates this concept, where terahertz and optical pulses are focused collinearly together, with their polarization aligned parallel to the modulated E_{bias} field. The second harmonic induced by E_{bias} acts as the local oscillator for heterodyne detection [12] that can be used to perform phase sensitive detection. Figure 4(b) plots the detected second harmonic intensity as a function of normalized third order nonlinear susceptibility $\chi^{(3)}$ along with a quadratic fit [6,20]. We can see that C_6H_{14} provides more than 243 times the sensitivity compared with N_2 or air. Using gases with larger $\chi^{(3)}$, elevated pressure (effective $\chi^{(3)}$ is proportional to the number of molecules), and higher probe pulse energy can help to optimize the sensitivity of the air-plasma detector [6].

2.2 Terahertz air photonic system electronics

The broad range of applications for air photonic systems has already yielded commercially available systems that utilize air-plasma as the source. One example is a recent system released by Newport Corporation [21]. The Newport system utilizes air-plasma for terahertz wave genera-

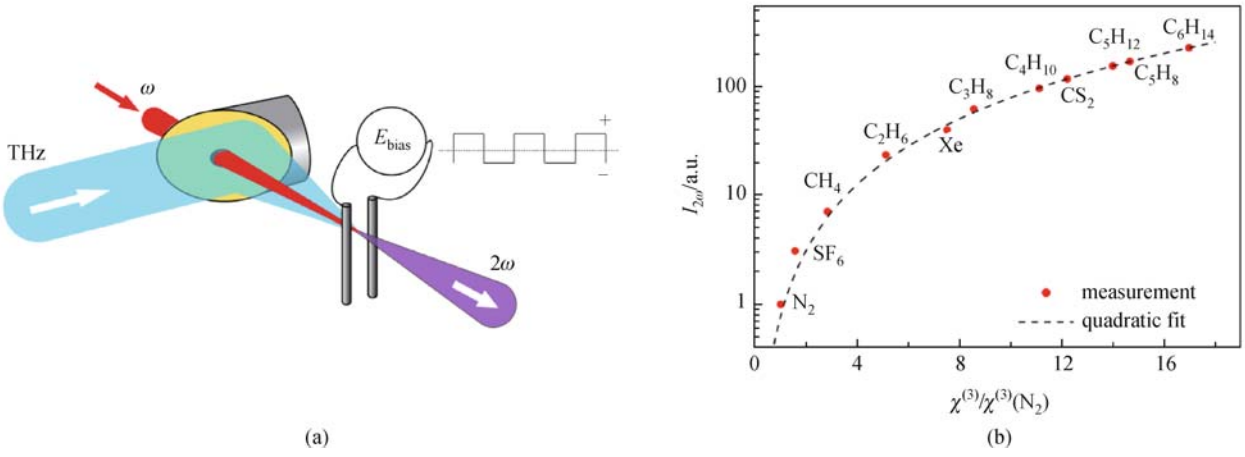

Fig. 4 (a) Basic concept of THz-ABCD: electrodes are placed at the geometric focus of collinearly focused terahertz and optical probe beams with a variable time delay. Second harmonic light is induced from the terahertz field and the local bias field E_{bias}. Modulating E_{bias} allows for heterodyne detection for enhanced sensitivity; (b) measured second harmonic intensity vs. third order nonlinear susceptibility $\chi^{(3)}$. All $\chi^{(3)}$ are normalized with respect to nitrogen. Data in (b) courtesy of Dr. Xiaofei Lu

tion, however the detectable bandwidth is limited to 3 terahertz since an electro-optic ZnTe crystal is used for detection. While for the nonlinear four wave mixing process, it is necessary to supply a high field local oscillator for coherent detection. This can be achieved electronically in two ways. The first method is to produce a high voltage square wave, triggered by an input signal, such as the laser transistor-transistor logic (TTL) output signal. The second method is to produce a high voltage pulse, where the timing of the pulse becomes important relevant to when the optical pulse arrives between the pair of biasing electrodes. The following sections describe square and pulsed high voltage modulator designs that we successfully prototyped, one of which was later developed into a commercially available product sold by Zomega Terahertz Corporation.

2.2.1 Square wave high voltage modulator

A strong local oscillator electric field is necessary for coherent terahertz wave detection through air-photonics as seen from Eq. (2), making the supporting high voltage electronics an invaluable tool in the system. For high voltage modulation, there are several things that need to be considered. Firstly, the more sensitive digital and analog control circuitry need to be isolated from high voltage potentials to minimize cross talk that can potentially interrupt circuit functionality. Secondly, attention to packaging and safety become important factors since large voltages are present at all times on the board. Thirdly, it is necessary to engineer the switching of these high voltages on the board without damaging the internal circuitry. As shown in the 3D rendered prototype in Fig. 5, the digital, analog, and high voltage electronics were all housed within a small aluminum box. The front panel uses a backlit liquid crystal display (LCD) to display voltage outputs, and a digital rocker switch to adjust the amplitude, phase, and modulation frequency.

The rear panel contains a heat exhaust fan, a CH1, CH2, and COM banana plug connection for interfacing the

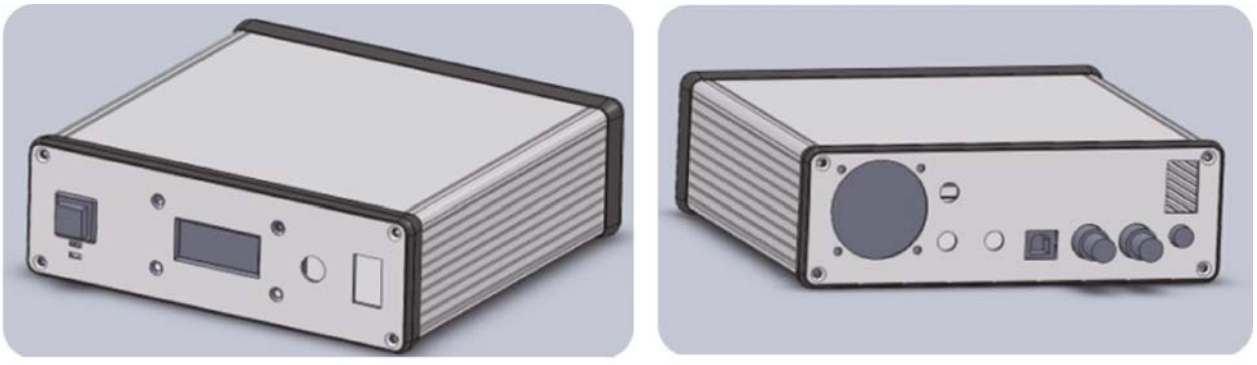

Fig. 5 3D-rendered Solidworks model of high voltage square wave modulator

switched high voltage output to a pair of electrodes in the THz-ABCD system. A universal serial bus (USB) interface is installed for optional communication and control of amplitude, phase, and frequency via a computer host. Additionally, the rear panel contains a TTL input and output reference signal for phases sensitive detection using a lock-in amplifier, a 12 volt power supply port for powering the device, and an ON/OFF toggle switch for immediate on and off control of the unit.

2.2.1.1 High voltage switching

The DC high voltage (HIGH V) is created using a commercially available DC to DC converter sold by EMCO that steps a 12V DC input up to the kilovolt level. Voltage switching was accomplished by implementing a full bridge N-channel metal-oxide-semiconductor field-effect transistor (MOSFET) design as depicted in Fig. 6.

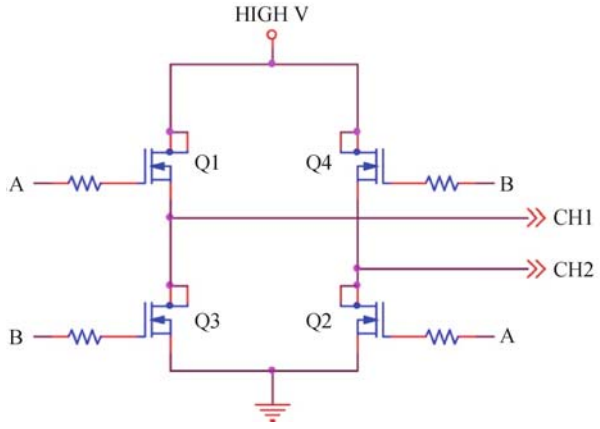

Fig. 6 N-channel MOSFET full bridge topology used for switching voltages with drive signals A and B

When the "A" signal is held high, MOSFETs Q1 and Q2 are turned on and CH1 becomes the potential of HIGH V, while CH2 becomes the potential of ground. Alternatively, when "B" signal is held high, MOSFETs Q3 and Q4 are turned on and CH1 becomes grounded while CH2 becomes the potential of HIGH V. If the CH1 and CH2 connections are connected to a pair of electrodes, the potential between them is simply their difference as shown in Fig. 7. This creates an alternating electric field between them at a selectable division of the input TTL signal, which in our case is determined by the amplified laser repetition rate of 1 kHz.

For lower voltages, the circuit design in Fig. 6 is adequate. However, since we desire to switch voltages on the order of several kilovolts, the commercial availability of high drain-to-source breakdown voltage field-effect transistors (FETs) becomes limited. In order to switch these kilovolt voltages, it becomes necessary to distribute the

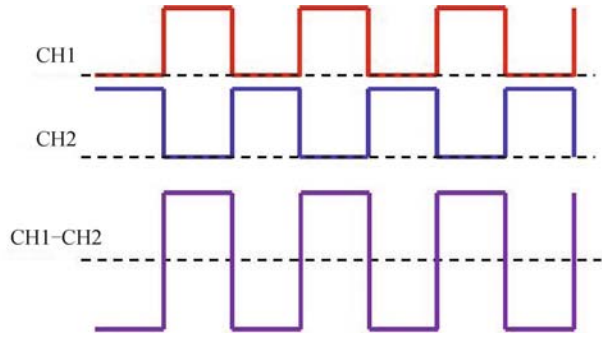

Fig. 7 Alternating voltage bias using an N-channel MOSFET bridge

voltage over a series of MOSFETS, switching them simultaneously to prevent breakdown. This was accomplished using an audio transformer with four separate 1:1 coils. The input signal at one coil is transformed into a potential across the other three windings, allowing for three separate MOSFET gates to be driven simultaneously. Varistors were used as protection circuitry to prevent any high voltage transient spikes that could potentially develop across the drain to source of the MOSFET if the gates are not switched at precisely the same time.

2.2.1.2 Operational testing

After construction, the device was tested at its maximum operating potential. Figure 8 shows the experimental test of the single-sided output using a 1/1000 resister divider to protect the oscilloscope probe breakdown voltage of 300 V. It can be seen that high voltage is switched relative to the TTL trigger input, meaning that each laser pulse receives a modulated bias at 1/2 the input frequency (500 Hz in our case). This means that the electric field orientation between the electrodes alternates between each pulse passing through the site of the electrodes.

It is important to note that the measurement made here is single-sided, meaning the potential is between CH1 and ground. If we looked at the potential between CH1 and CH2, we would see twice the potential of the single sided measurement with an alternating electric field direction as depicted in the lower portion of Fig. 7. The alternating field is used as a local oscillator for coherent terahertz wave detection. The prototype, later developed into a commercial product, is shown in Fig. 9, and is available through Zomega Terahertz Corporation [22].

2.2.2 Pulsed high voltage modulator

The alternative for creating a high voltage local oscillator for use in air photonics is to create short pulses of high voltage. The advantages of using a pulsed system are not only size reductions, since compact high quality factor

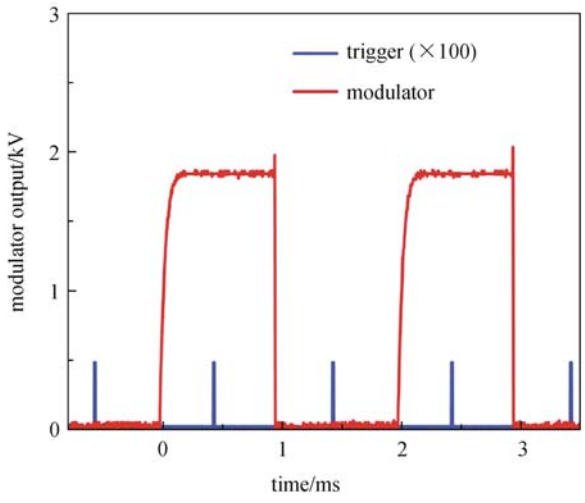

Fig. 8 Square wave high voltage modulator operating at maximum output voltage as determined by the DC-DC converter. The laser TTL output is sent to the modulator and a voltage divider is used to monitor the CH1 output. When operating with electrodes, the total output potential is CH1–CH2, twice that shown

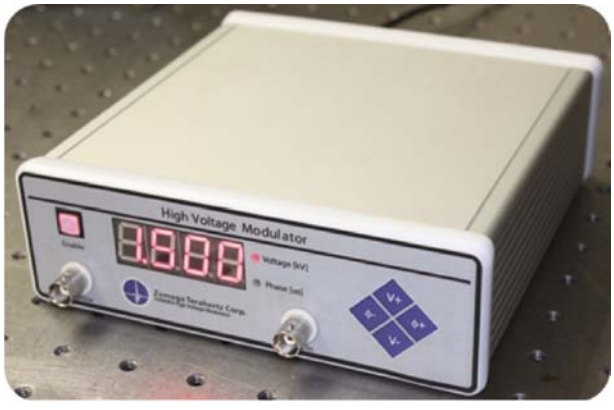

Fig. 9 Commercialized high voltage square wave modulator sold through Zomega Terahertz Corporation

transformers can be used to replace large DC-DC converters, but also the possibility to instantaneously generate high voltages with low level voltage inputs. This means there are only very short periods of time that have high voltage potentials on the board. The disadvantage of this system is that timing becomes very important, since the high voltage pulse must be present at the site of the electrodes during the passage of the optical pulse. A 3D rendering of the pulsed high voltage modulator prototype is shown in Fig. 10.

The pulsed system front panel has three main elements. From left to right: amplitude/phase selection switch with amplitude/phase indicator light emitting diode (LED); an LCD display; increment/decrement rocker switch for adjustment of phase and amplitude, and phase lock indicator LED. On the back, the prototype has a USB interface, a TTL input and output reference, a 12 volt power jack with an ON/OFF toggle switch, and a port for connection of the high voltage leads that interface to the electrodes.

2.2.2.1 Digital circuitry

For this system, a Texas Instruments MSP family microcontroller was used to perform functions such as analog to digital conversion and display of the amplitude and phase readings. A Xilinx computer programmable logic device (CPLD) was used to implement a digital phase-locked loop (PLL) to synchronize the laser TTL input signal with the internal oscillator used for adjusting the timing delay of the output pulse. The digital PLL was implemented in software as shown in Fig. 11.

A frequency divided output from a voltage controlled oscillator (VCO) and the laser TTL input are used as the input clock sources of the flops. If the clocks are not raised high simultaneously, a small pulse is sent to either the Freq_Up or Freq_Dn outputs of the Xilinx chip before the outputs of the flops are cleared. If the clock for both flops is raised simultaneously, the flops are not cleared and the

Fig. 10 3D rendered Solidworks model of pulsed high voltage modulator prototype

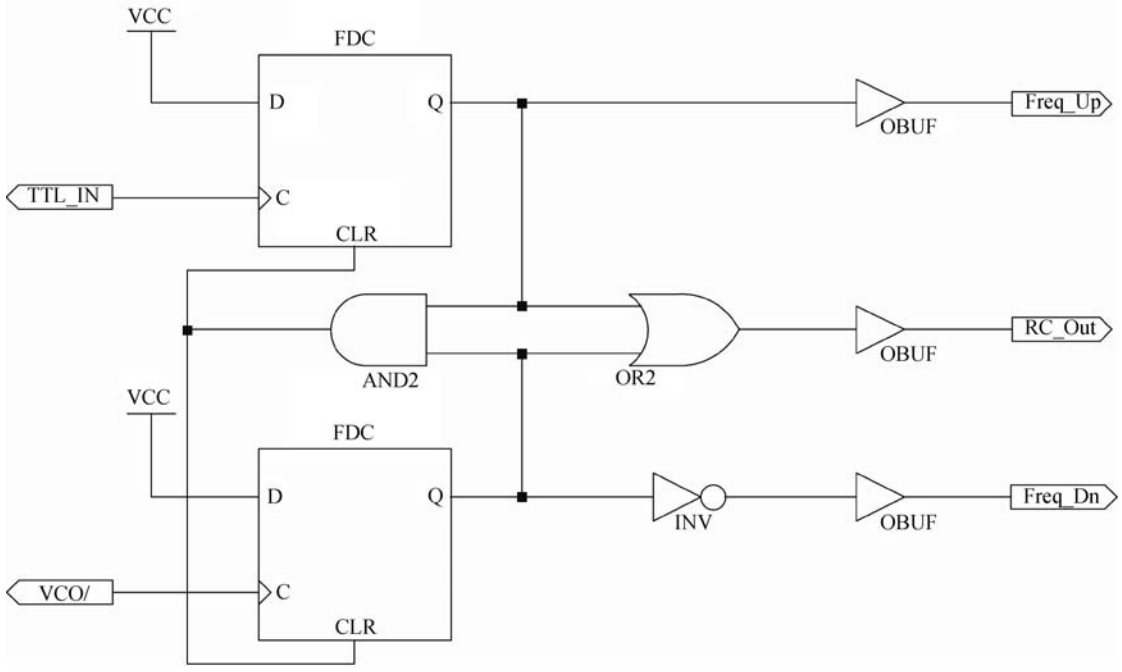

Fig. 11 Digital implementation of phase locked loop in a Xilinx CPLD to synchronize digital circuitry timing to laser trigger signal

resulting output is balanced, making RC_Out logic low which causes the phase lock LED to illuminate.

Once the digital circuitry clock has been synchronized to the reference laser trigger, the delay between an internally generated 1 kHz pulse train and the input trigger signal is controlled by using a 16-bit loadable cascadable bidirectional binary counter (DB16X1) with a 16-bit cascadable adder/subtracter (ADSU16). The adder has a constant time value loaded at startup to compensate for the time the optical pulse must propagate through the air to reach the electrodes. Additional phase adjustments are made by "tickling" the SETFREQ pin on the MCU to increase or decrease the delay between the input trigger and the output high voltage pulse. The MODENABLE pin on the MCU is reserved for controlling either increment or decrement functions. The phase delay adjustment digital circuitry implemented in the Xilinx CPLD is shown in Fig.12. Once the 16 bit counter (CB16CE) counts up to the desired delay value, the COMP16 comparator output goes high to initiate the output pulse. If the value of the delay timing is changed, the flash memory in the MCU is updated with the new value so that this timing is saved for the next time the device is turned on.

2.2.2.2 Analog circuitry

The external analog circuitry interfacing to the CPLD can be seen in Fig.13. The small voltage pulses from Freq_Up or Freq_Dn result in either charging or discharging of the capacitor C67, which determines the set voltage of the voltage controlled oscillator for synchronizing the internal oscillator to the reference signal.

In order to produce the high voltage pulses, the same technique is borrowed from the square wave modulator bridge design relating to Fig. 6. By using two separate pulses at the input of a transformer, it is possible to make the potential drop across the transformer look like twice that of the input voltage. In addition, by controlling the relative timing between the two input pulses, it is possible to change the output polarity of the high voltage spike as seen in Fig.14. Here a 1/1000 resistor divider is used to look at the output of the transformer that will be connected to the biasing electrodes.

Similar to the method for generating an alternating electric field with the square wave modulator in Fig. 7, it is important that the electric field alternates for the pulsed system. In order to flip the polarity of the high voltage pulse, the CPLD digital logic is programmed to alternate between the two timing scenarios shown in Fig. 14. A phase-locked output of the unit is shown in the experimental data presented in Fig. 15. It is this pulse train output that can be adjusted accurately in phase such that the peak of each high voltage pulse is aligned with the precise time that the combined optical and terahertz pulses exist between the electrodes in the THz-ABCD system.

Since the optical pulse lasts for only femtosecond time duration, even if the electric field pulse duration is on the order of nanoseconds, the voltage seen by the optical field

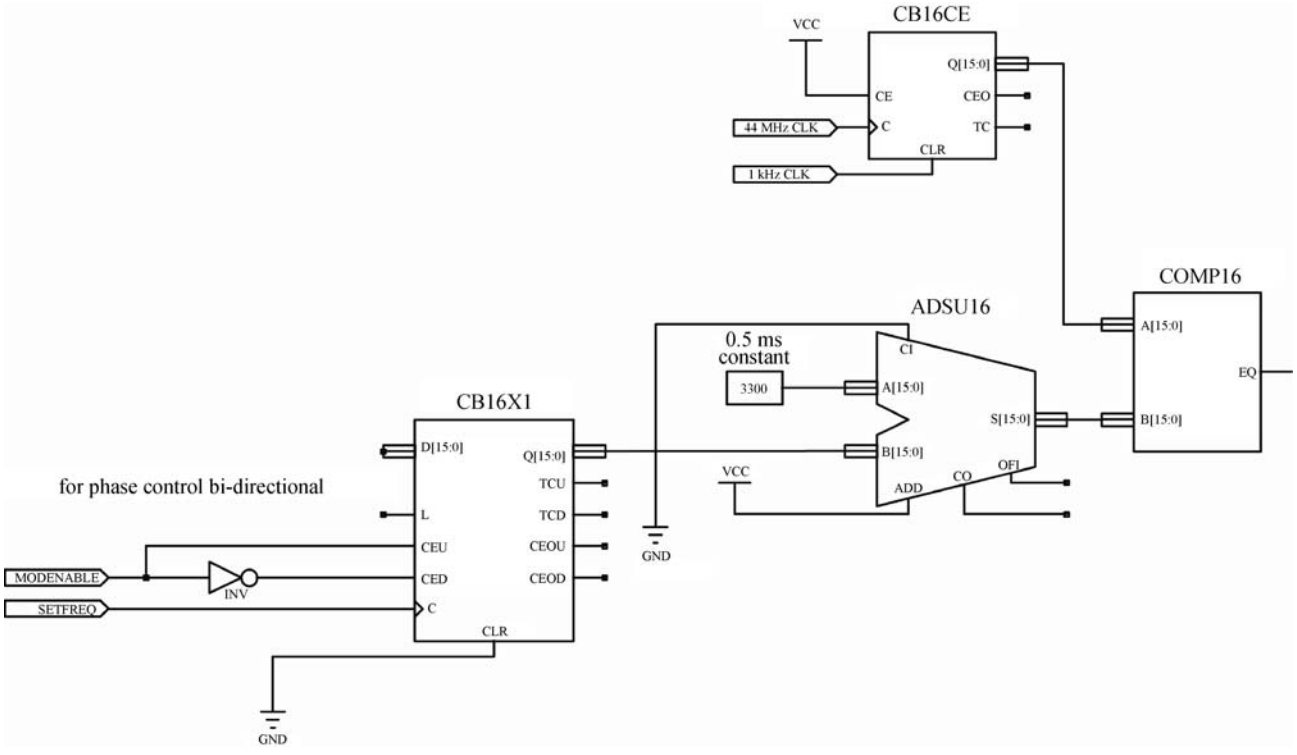

Fig. 12 Electronic pulse phase control circuitry implemented in the Xilinx CPLD. CB16X1: 16-bit loadable cascadable bidirectional binary counter; CB16CE: 16-bit cascadable binary counter; ADSU16: 16-bit cascadable adder/subtracter; COMP16: 16-bit Identity Comparator

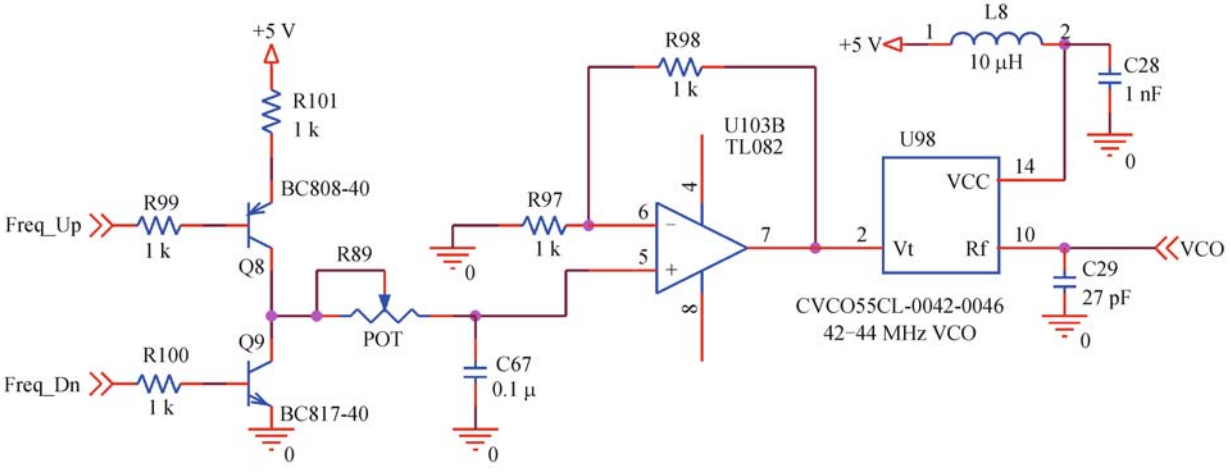

Fig. 13 Analog circuitry interfaced to Xilinx CPLD for phase locked loop

will appear to be constant, meaning any following oscillations are irrelevant to the detection process and can actually benefit the user when finding the initial system timing.

2.2.3 Summary

Two high voltage modulator prototypes were developed to be used with the terahertz air photonic system that utilizes nonlinear photomixing of terahertz and optical photons, in combination with a high-strength local oscillator field, to perform coherent terahertz wave detection in air. It can be seen that there are benefits to each system. The square wave modulator electronics design is by far more simplistic, since the electronic pulse timing is unimportant (phase can be set to anything other than right at the

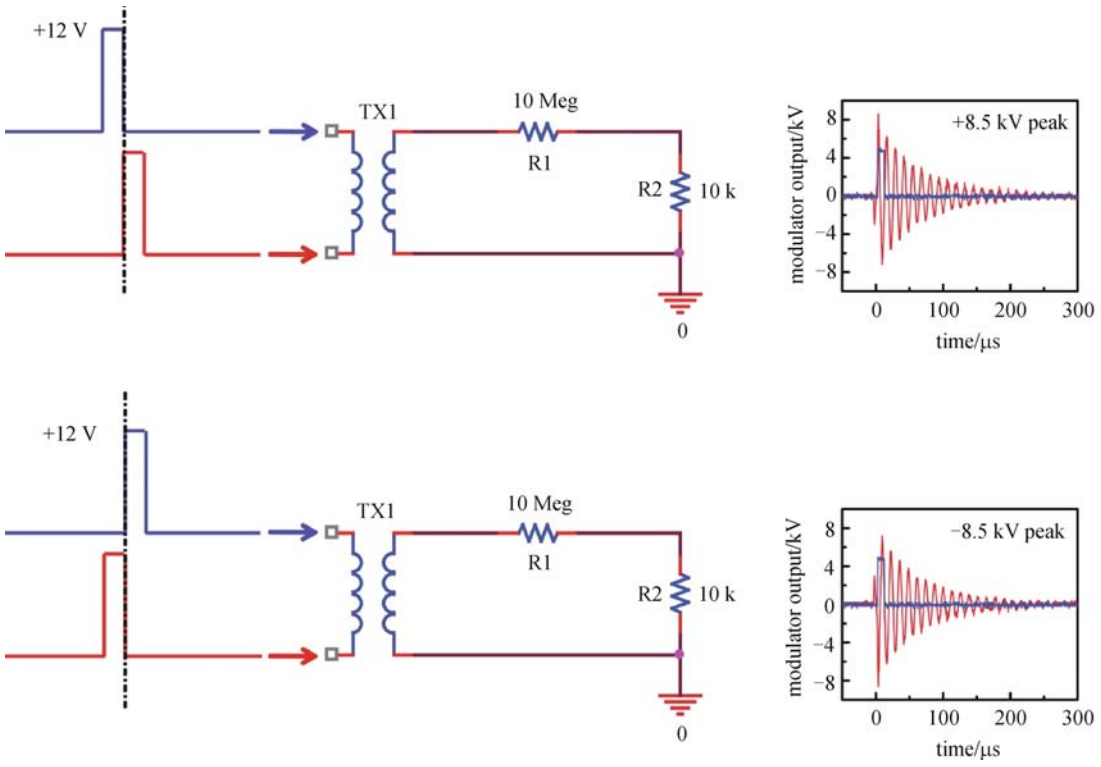

Fig. 14 A compact, high *Q*-factor, high turns-ratio transformer is pulsed using the output from the MOSFET bridge. The polarity of the high voltage output pulse is determined by the input pulse timing

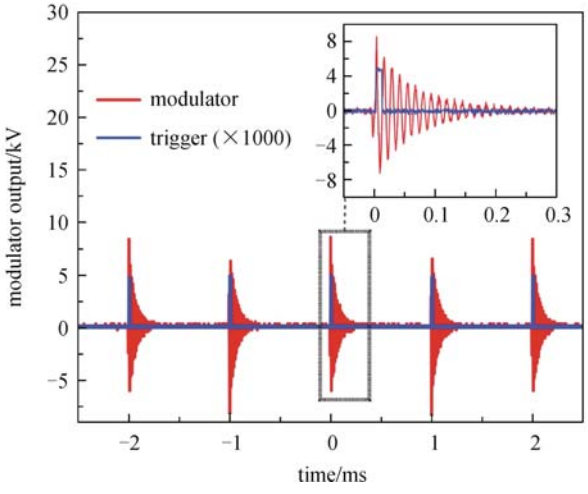

Fig. 15 Phase-locked output of pulsed high voltage modulator showing filed polarity altering between each trigger from the reference

transition). Although the pulsed system requires more complex circuitry, it has a more compact form factor, and results in higher possible voltage outputs due to its transient nature. It is also considered a safer device since the nanosecond high voltage transients are only present at the output for short periods of time rather than the constant high voltages that exist on the circuit board at all times with the square wave modulator.

2.3 Terahertz detection through air-plasma fluorescence

Due to the composition of gasses in air, as free electrons in the plasma relax to lower energy states through the recombination with ions, visible fluorescence is emitted which can be modulated by an external electromagnetic pulse. The external field influences the number of fully ionized states through collisional excitation of bound high-lying Rydberg states, yielding information about the external instantaneous field in the form of fluorescence changes. Therefore, terahertz signals can be detected indirectly through observation of the terahertz-radiation-enhanced-emission of fluorescence, a technique nicknamed (THz-REEF) [23]. It is therefore possible that terahertz spectroscopic “fingerprints” of materials can be encoded into fluorescence (300–450 nm) wavelengths, advantageous due to their transparency during atmospheric propagation and low detectible signal levels using highly sensitive optical sensing equipment. In a previously conducted THz-REEF experiment, shown in Fig. 16(a), a terahertz pulse propagated through the plasma and the fluorescence was measured by a spectrometer. By increasing the kinetic energy of electrons through terahertz-field acceleration in the plasma, as illustrated in Fig. 16(b), fluorescence emission could be enhanced. Figure 16(c) shows the nitrogen fluorescence spectra with and without the terahertz field imposed on the gas-plasma.

When two-color pulses (800 and 400 nm) are super-

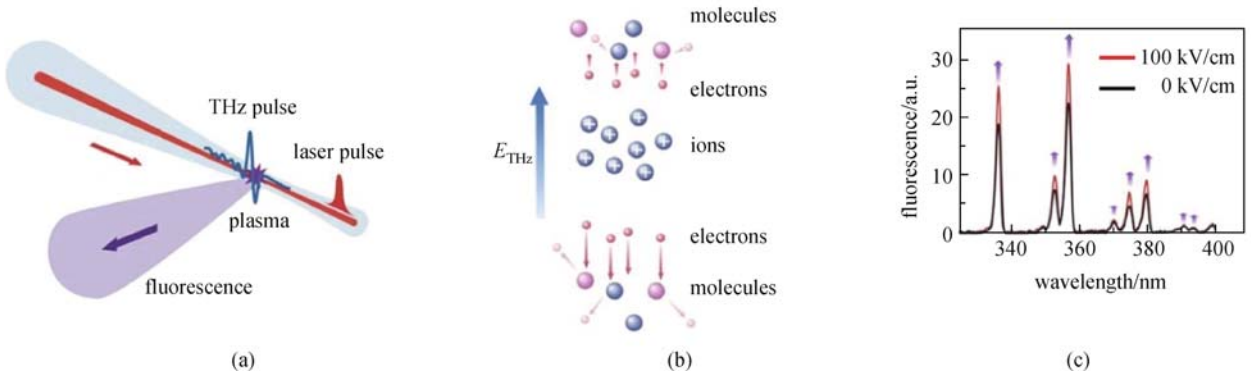

Fig. 16 (a) Experimental geometry for THz-REEF from air-plasma using a single-color laser pulse excitation; (b) electron acceleration in the terahertz field and collision with neighboring molecules; (c) THz-enhanced fluorescence spectra of nitrogen gas-plasma under influence of 100 kV/cm peak field. © IEEE, reprinted, with permission from Ref. [24]

posed to form a plasma, the ionized electrons' net drift velocity becomes a function of the relative phase between the pulses [8]. Electron motion can be symmetric, parallel, or anti-parallel to the terahertz wave polarization by changing the relative phase of the pulses. Once the terahertz pulse arrives, electrons are driven to move faster (if $E_{THz}(t)$ is anti-parallel to the initial velocity) or slower (if $E_{THz}(t)$ is parallel). Figure 17(a) shows the time-resolved air-plasma fluorescence for the parallel, symmetric, and antiparallel electron drift velocities as the terahertz pulse interacts with the plasma.

In each scenario, there is fluorescence enhancement, but each contains unique "features" from either the increase, constant, or decrease in electron velocity (and therefore energy transfer) by the terahertz field [25]. Figure 17(b) shows the coherent terahertz waveform revealed in the fluorescence by subtracting the parallel curve from the antiparallel curve. The THz-REEF signal thus allows for terahertz wave coherent detection, meaning air-plasma fluorescence can also indirectly give information regarding a material.

2.4 All air-plasma terahertz spectroscopy

Among many important applications of terahertz radiation in science and industry, it is fair to say that terahertz time domain spectroscopy (THz-TDS) has become a highlight due to its exceptional ability to excite vibrational and rotational modes within organic materials, including but not limited to explosive compounds [26]. Although terahertz spectroscopic "fingerprinting" has proved to be an exceptional method for material characterization [27,28], these classifications require solid state materials such as electro-optic crystals or electrodes that must be

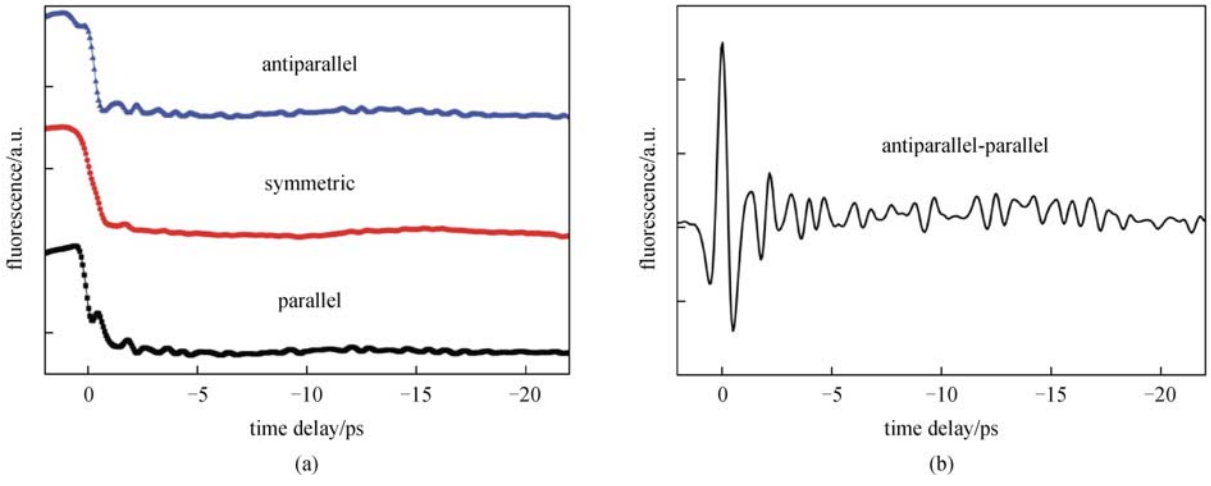

Fig. 17 (a) Time-resolved air-plasma fluorescence enhancement from terahertz wave interaction with antiparallel, symmetric, and parallel electron drift velocities with respect to the laser field, controlled by changing the relative phase between the ω and 2ω optical pulses; (b) subtracting the parallel curve from the antiparallel curve removes the incoherent energy transfer by electrons after inelastic collisions and scattering in random directions. This reveals the terahertz waveform in the form of fluorescence modulation. The optical pulse leads the terahertz pulse in time for delay $t_d < 0$

used in conjunction with the laser pulse for generation and detection [12,14,15,29]. Furthermore, current terahertz detection methods require the detector to collect information of the terahertz wave in the forward propagating direction; information regarding the terahertz transient is unable to be retrieved in the backwards direction. It is also impractical to send terahertz waves directly to the sample through the atmosphere due to fundamentally large water vapor attention [30]. For these reasons, terahertz spectroscopic measurements have all taken place under purged nitrogen environments, or at extremely short distances where the operator remains exposed to the potential hazards under study. Remote terahertz spectroscopy remains somewhat a "holy grail", since it would enable non-invasive material identification from a safe distance.

In this section, an "all air-plasma" terahertz spectroscopy system is introduced, that encodes explosive signatures of Nitroguanidine (NG), 2,4-Dinitrotoluene (2,4-DNT), and Cyclotetramethylene tetranitramine (HMX) into the nitrogen fluorescence emitted from a bichromatic laser-induced plasma filament using fluorescence detection principles discussed previously. Since the plasma filament serves as both the terahertz emitter and detector, terahertz pulse detection is no longer restrained by electrodes, solid state materials, or forward signal collection; showing the feasibility for conducting remote terahertz spectroscopy. We show that broadband terahertz pulses emitted from a plasma filament source, and the omnidirectional nitrogen fluorescence from a two-color plasma filament can carry spectroscopic information regarding terahertz-material interaction.

2.4.1 Prior efforts for remote terahertz wave sensing

In 2009, Dai and Zhang demonstrated remote terahertz wave generation by focusing two optical pulses into air at 17 meters from the last optic to form a plasma that emitted broadband pulses of terahertz radiation [31]. An in-line phase compensator, preceding the large diameter focusing mirror, was used to mechanically stabilize and adjust the phase between the fundamental and second harmonic laser pulse [32]. In 2010, Wang et al. demonstrated a similar measurement obtaining terahertz pulse energies larger than 250 nJ [33]. Both demonstrations show the ability for generating intense terahertz radiation at remote distances; however, the problem remains carrying coherent information regarding the terahertz electromagnetic pulse back to the user. More recently, as proof of concept, we showed that single-cycle terahertz pulse information could be encoded into laser-induced plasma nitrogen fluorescence and acoustic waves [25,34,35]; however, these demonstrations both used a solid state $LiNbO_3$ crystal for the terahertz wave source, and therefore the system was restricted to local distances with a system bandwidth less than 3 terahertz.

2.4.2 Experimental setup

Here all air-plasma terahertz spectroscopy is demonstrated, utilizing nitrogen fluorescence encoding, which is performed using laser plasmas for both the terahertz wave emitter and detector as would be necessary for remote operation. Figure 18 shows the pump-probe experimental layout. Of the total 700 μJ system input pulse energy, 70% was sent to the pump to generate terahertz waves through two-color ionization of the air [2,8,36]. The remaining 30% was used to generate a plasma detector from which the nitrogen fluorescence was monitored. A 100 μm thick type-1 β-BBO crystal was used to generate second harmonic pulses from the 80 fs 500 μJ optical pump pulses. The terahertz pulse energy was estimated to be 50 nJ (limited only by laser input energy) using a calibrated pyroelectric detector. Field strengths of 40 kV/cm were produced from the generation plasma as measured by electro-optic sampling techniques [14]. In comparison, over 300 nJ pulse energies were generated through the tilted pulse front method used for initial plasma acoustic and fluorescence encoding demonstrations. An in-line phase compensator [32] controlled the relative phase between the 800 and 400 nm pulses, and moreover the electron trajectory inside the bichromatic field-induced probe plasma [8].

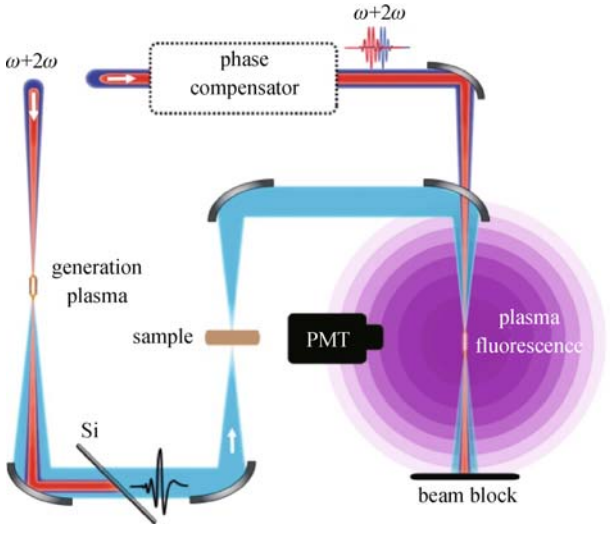

Fig. 18 "All air-plasma" terahertz spectroscopy system. Air-plasma filaments are used for both generation and detection of the terahertz electromagnetic radiation. (Light blue: terahertz), (Red: 800 nm pulse), (Blue: 400 nm pulse), (Purple: nitrogen fluorescence). Nitrogen fluorescence emitted from the probe plasma carries the encoded terahertz pulse information

Terahertz radiation from the air-plasma source was collected and refocused through a pair of 3″ off-axis parabolic mirrors (OAPM) for testing samples in transmis-

sion geometry. The transmitted terahertz energy was refocused collinearly with the two color probe pulses using a 2″ OAPM.

2.4.3 Experimental results and discussion

A photomultiplier tube with a (354±10) nm filter was used to monitor the probe plasma nitrogen fluorescence at 357 nm while the delay between terahertz and optical pulses was scanned. Figure 19(a) shows the coherent terahertz pulse after decoding the nitrogen fluorescence using techniques discussed in reference [25]. A waveform in Fig. 19(a) and spectra in Fig. 19(b) of the same pulse recovered using a 100 μm thick GaP electro-optic crystal, is showed for comparison, indicating congruency between the respective methods.

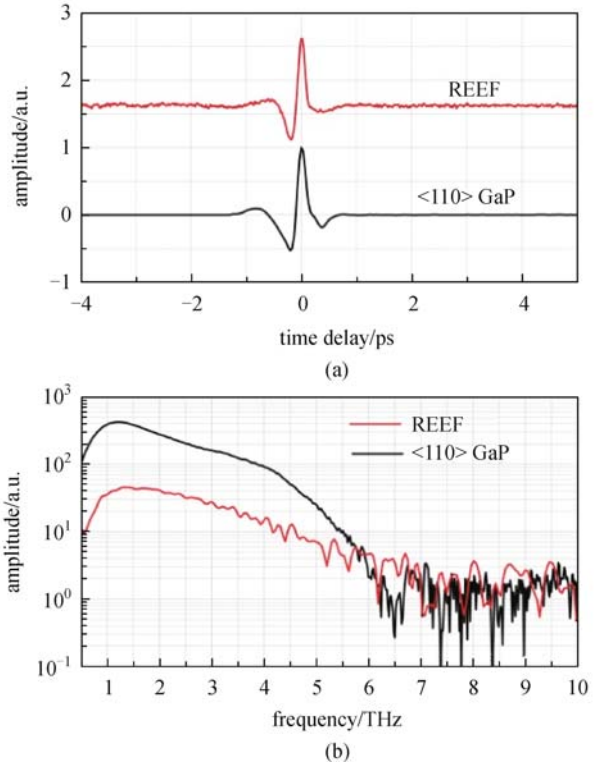

Fig. 19 (a) Terahertz pulses recovered from the radiation-enhanced-emission of fluorescence (REEF) and electro-optic sampling method using a 100 μm thick <110> GaP crystal; (b) corresponding spectrum after Fourier transformation

Since the THz-REEF technique does not require solid state materials for detection, the useable bandwidth is not limited by material phonon resonance, but only by optical pulse duration. In order to demonstrate the broadband spectroscopic capability of this method, spectroscopic signatures of NG, 2,4-DNT, and HMX were encoded into the nitrogen fluorescence, using experiments in which the samples of these three explosive materials interacted with a pulsed terahertz signal. The respective electro-optic measurements were performed to validate the reliability of the method. Although not specifically necessary, measurements described here were performed under dry nitrogen purged conditions to elucidate explosive sample absorbance signatures and increase the system signal-to-noise ratio (SNR) for reduced averaging times. Figures 20 (b) and 20(d) compare the absorbance information using fluorescence encoding and electro-optic sampling methods.

The spectroscopic features of all chemical compounds are sufficiently resolved by the two methods. Slight variations in the terahertz waveform and absorption signatures were expected due to small differences in sample positioning and terahertz-optical beam overlap in the plasma or electro-optic crystal, however, the absorption peak locations show good agreement between the respective methods and the existing literature values [37,38].

Each sample was prepared by uniformly mixing micrometer grain size polyethylene powder containing 20% of the explosive compound. The samples were compressed at 9 metric tons for 3 minutes and were all less than 1 mm thick. For these measurements, sample preparation was important due to laser power limitations and therefore available terahertz pulse energy. A compromise between the system SNR and sample absorbance had to be made. Samples containing larger than 20% chemical concentrations undoubtedly produced more noticeable absorption features; however, this came at the penalty of reduction in transmitted terahertz energy and therefore a substantial decrease in the fluorescence measurement SNR. For this reason, all chemical concentrations were limited to 20%, which allowed for more than 50% transmission of the terahertz peak electric field.

3 Terahertz enhanced acoustics

Until recently, the generation and detection of terahertz waves using laser air photonics has taken place on an optical table bench, where a combination of carefully positioned optics and electronics have been fused to perform broadband terahertz spectroscopy. In this part, a new concept is discussed that aims to push the capabilities of table-top air photonic terahertz systems beyond the lab bench to a remote site, where carefully positioned optics and electronics can no longer be used. By “listening” to laser-induced plasma, it becomes feasible to carry information of terahertz waves through the atmosphere in an isotropic geometry. Although many technical challenges remain, this unique technique presents another large step toward realizing a remotely operational terahertz spectrometer; opening new scientific directions and opportunities for electromagnetic sensing.

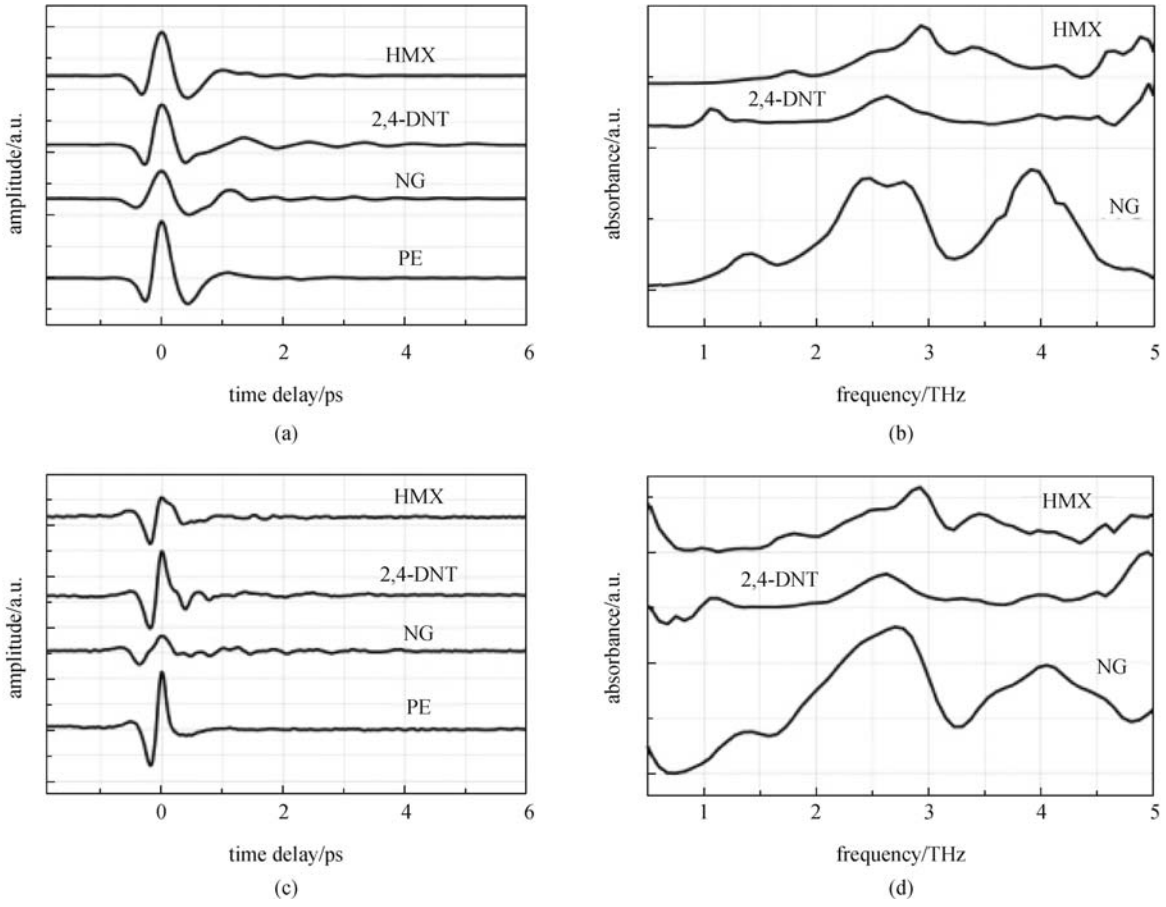

Fig. 20 (a) Terahertz waveforms for pellet samples NG, 2,4-DNT, and HMX containing 20% chemical mixed with polyethylene obtained using electro-optic sampling; (b) absorbance signatures corresponding to samples in (a); (c) identical samples and corresponding waveforms obtained using radiation enhanced emission of fluorescence (REEF) encoding; (d) absorbance signatures corresponding to samples in (c). All curves are offset for clarity

3.1 Theoretical model

Under the irradiation of intense optical fields, such as high-power femtosecond laser pulses focused into air, the molecules are ionized, meaning free electrons are released from their parent molecules once the laser field overcomes the atomic Coulomb potential. After being ejected from the atoms or molecules during the leading part of the laser pulse, the electrons are accelerated by the remainder of the laser pulse and drift away from their parent ions. In the intense laser field excitation, the electron temperature is usually much higher than the temperature of the neutral particles (mostly molecules in air and ions whose mass are generally thousands of times larger than the electron mass). Before the electron-ion recombination, these "hot" electrons collide with the neighboring "cold" molecules and transfer some portion of kinetic energy through inelastic electron-molecule collisions in the following nanoseconds [39]. The subsequent translational motion of the molecules gives rise to the creation of a shock wave, which then relaxes into an acoustic wave [40–42].

While when a terahertz wave irradiates the plasma, the terahertz field can modify the plasma acoustic pressure by changing the electron velocity and therefore kinetic energy transfer to the plasma. To study the influence of terahertz waves on plasma acoustics, a theoretical model containing laser-induced photoacoustics and kinetics of electrons and molecules in the terahertz field is constructed here. Acoustic wave propagation in the presence of a heating source can be written as [43]

$$\left(\nabla^2 - \frac{1}{c_s^2}\frac{\partial^2}{\partial t^2}\right)p(r,t) = -\frac{\beta}{C_p}\frac{\partial H(r,t)}{\partial t}. \quad (3)$$

Here, the sound velocity, c_s is assumed to be constant after thickening of the shock, for which the wave is restored to the linear region [44,45]. The β and C_p are the isobaric volume-expansion coefficient and heat capacity per unit mass at constant pressure respectively, and $p(r,t)$ is the acoustic pressure (deviation from atmospheric). $H(r,t)$ is the heating function, defined as the rate of the heat transfer from electrons into molecular translational energy,

where

$$H(r,t) = n_e E_T h(r,t) \propto (n_e m_e v_e^2/2) h(r,t).$$

The $h(r,t)$ term is determined by the nature of the energy transfer process and is a complex function of gas density and laser intensity. Here, n_e is the free electron density. E_T is the total energy transferred from each electron to neighboring air molecules in the single-electron approximation, where electron-electron interaction is neglected. The solution of Eq. (3), $p(r,t)$, can be expressed as

$$p(r,t) = n_e E_T f(r,t) \propto (n_e m_e v_e^2/2) f(r,t), \quad (4)$$

where $f(r,t)$ can be obtained using the Green's function solution of Eq. (3), together with $h(r,t)$ [43], and its specific expression is not of much concern since only its dependence on electron temperature is of interest here.

When the plasma is subjected to an external terahertz field $E_{THz}(t)$, the acceleration of free electrons and the following electron-molecule collisions give rise to a local plasma temperature increase. This temperature increase results in the enhanced acoustic emission from the plasma. The energy transfer, E_T, is therefore increased to $E_T + \Delta E_T$ through terahertz-induced electron heating. Since the electron relaxation time, τ, at atmospheric pressure is small in comparison to the terahertz pulse duration [46], the terahertz waveform can be "segmented" into many small pieces, within which the terahertz field is considered constant. This treatment would simplify the calculation of terahertz-driven electron motion. Therefore, the pressure enhancement $\Delta p(r,t,t_D)$ can be approximated as

$$\Delta p(r,t,t_D) = n_e \Delta E_T(t_D) f(r,t) \propto n_e m_e \sum_{i=1}^{\infty} \left(\Delta \vec{v}_{e_i}\right)^2$$

$$= \frac{e^2 n_e \tau}{m_e} \int_{t_D}^{\infty} \vec{E}_{THz}(t')^2 dt', \quad (5)$$

where n_e can be treated as a constant since the terahertz pulse duration is much shorter than the electron-ion recombination time, which is on the scale of nanoseconds [47]. The time delay between the terahertz pulse and the laser pulse is t_D, and its sign is defined so that t_D is positive when the terahertz pulse leads the optical pulse in time, and negative when the terahertz pulse is behind the optical pulse. $\Delta \vec{v}_{ei}$ is the change of the electron velocity by the terahertz field during the time period between the $(i-1)$th and the ith electron-molecule collision. Here, $\Delta \vec{v}_{ei} = -\int_{t_i-\tau}^{t_i} e \vec{E}_{THz}(t') dt'/m_e$. Furthermore, the magnitude of the enhancement ratio is described as

$$\frac{\Delta p}{p} = \frac{m_e \sum_{i=1}^{\infty} \left(\Delta \vec{v}_{ei}\right)^2}{m_e \vec{v}_e^{\,2}/2}, \quad (6)$$

where, for a 100 kV/cm peak terahertz field, the maximum $m_e \sum_{i=1}^{\infty} (\Delta \vec{v}_{ei})^2 = \frac{e^2\tau}{m_e} \int_{t_D}^{\infty} \vec{E}_{THz}(t')^2 dt'$ is estimated to be 0.3 eV in the limit of very short relaxation time (i.e., τ is much smaller than the terahertz pulse duration). The initial electron kinetic energy $m_e \vec{v}_e^{\,2}/2$ is estimated to be several eV for the laser intensity of 10^{13} ~10^{14} W/cm^2 [48]. From this theoretical model, it can be seen that acoustic emission from a laser-induced plasma might serve as an electromagnetic sensor.

3.2 Experiments and discussion

According to the theoretical predictions above, we experimentally investigate the terahertz wave detection by using photoacoustics. The methods include incoherent and coherent detection.

3.2.1 Incoherent detection

In the experiment illustrated in Fig. 21(a), a single-color (800 nm, 80 fs, 110 μJ pulse energy, 1 kHz repetition rate) optical pulse was focused into the air to produce an acoustic pulse. The total laser intensity at the focus was 10^{13}~10^{14} W/cm^2. Under illumination of an intense femtosecond laser pulse, photoionization of the molecules takes place in the sub-picoseond time scale as the laser field overcomes the Coulomb potential binding the electrons to their parent atoms. The laser field increases the free electron temperature, T_e, to 10^4~10^5 K, while neighboring molecules or ions have a much lower temperature, T_m [48]. In the following 10^{-8}~10^{-9} s, T_m is gradually increased through energy transfer from collisions between hot electrons and their surrounding air molecules until thermal equilibrium is achieved [39,49]. This rise in localized gas temperature produces a shock wave that persists for a short distance [50], before relaxing into an acoustic wave [41].

The waveform of the acoustic pulse was measured with a broadband microphone (G.R.A.S 40DP). A single-cycle terahertz pulse with peak field of approximately 100 kV/cm, generated using the tilted pulse front optical rectification technique in $LiNbO_3$ [29], was spatially and temporally overlapped with the optical pulse. When the adjustable time delay between the terahertz pulse and optical pulse, 't_d' in Fig. 21(a), was negative (optical pulse preceding the terahertz pulse), a 10% amplitude enhancement of the sound pressure in the entire waveform was observed. Figure 21(b) shows the measured acoustic waveforms with and without the 100 kV/cm terahertz field incident on the plasma. The corresponding inset shows the terahertz-induced pressure enhancement in the frequency domain (up to 140 kHz) after Fourier transformation of the single-pulse waveforms.

Furthermore, a pair of wire grid polarizers, with 1000:1 extinction ratio and bandwidth from 0 to 4 terahertz, was used to determine the acoustic enhancement dependence on the terahertz wave. The angle between the first polarizer and the vertical direction, θ, is tuned, while the second

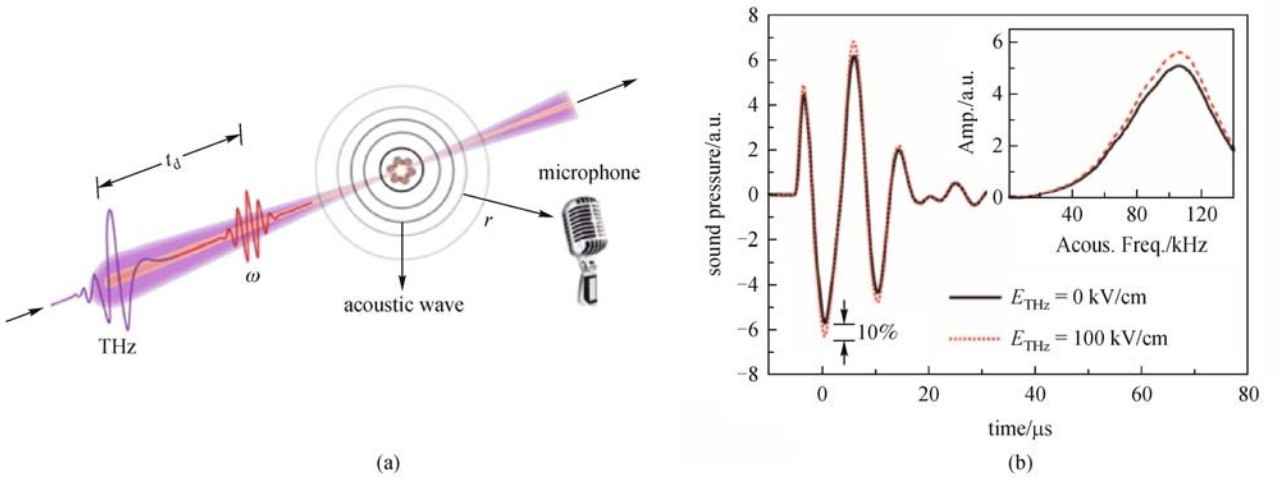

Fig. 21 (a) Experimental setup for performing terahertz enhanced acoustics using single-color femtosecond laser excitation; (b) single photoacoustic waveforms measured at 5 mm distance with (red-dashed) and without (black-solid) a 100 kV/cm terahertz field. The insert shows the acoustic spectra in linear scale. Amp.: amplitude; Acous. Freq.: acoustic frequency

polarizer is fixed at 90° and transmits the vertical component of the terahertz wave. Thus, after passing two polarizers, the terahertz wave is kept vertically polarized and the amplitude of the terahertz field is $E_{\mathrm{THz}}\cos^2(\theta)$ and the amplitude of the terahertz intensity is $I_{\mathrm{THz}}\cos^4(\theta)$. The measured results (red dots) and quadratic fit (dashed blue line) are shown in Fig. 22, in which the observed quadratic dependence is also consistent with the terahertz field squared term in Eq. (5).

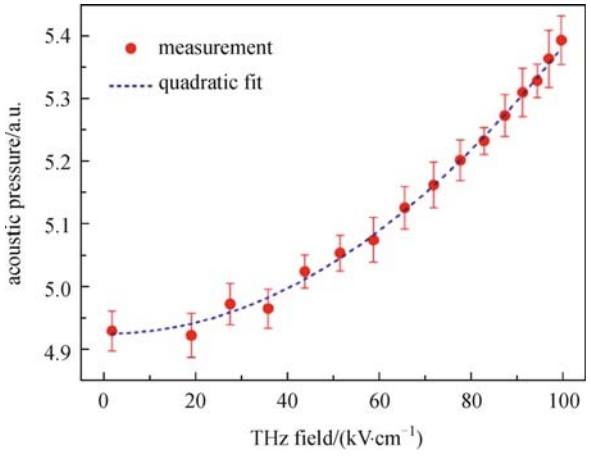

Fig. 22 Measured terahertz field dependence of acoustic pressure (red dots) at 100 kHz and quadratic fit (blue dashed line)

Besides, to study laser-induced photoacoustic dynamics under single-cycle terahertz radiation, the acoustic signal at 100 kHz was measured by varying the time delay t_d. The results are shown as the solid curve in Fig. 23. In region I, the terahertz pulse leads the optical pulse in time and there is no acoustic enhancement, because there is no interaction between the terahertz pulse and the plasma; however, when the field of the terahertz pulse begins to interact with the plasma, a sharp rise in the acoustic signal is observed, with the period of rising time comparable to the width of a single-cycle terahertz pulse. In region II, following the rise, a slow decay of the acoustic signal on the order of nanoseconds is observed and agrees with the temporal profile of the electron density decay due to electron-ion recombination [47].

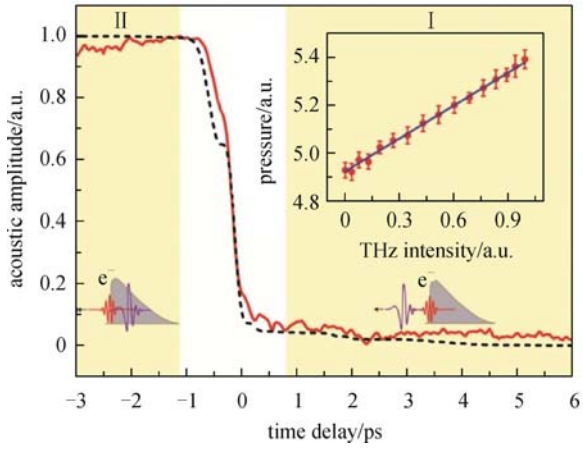

Fig. 23 Normalized pressure enhancement signal at 100 kHz as a function of time delay t_d. Region I: terahertz pulse leads the optical pulse in time; region II: terahertz pulse trails the optical pulse in time. The dashed line is the calculated signal. Inset shows the acoustic signal at 100 kHz for different terahertz intensities incident on single-color laser-induced plasma and a linear fit

Additionally, a lock-in amplifier measured the acoustic signal at 100 kHz, using the 100th harmonic of the laser repetition rate (1 kHz). The inset of Fig. 23 shows the acoustic enhancement at 100 kHz for different terahertz intensities. Good agreement between the measurement and

linear fit shows that the enhanced acoustic pressure is linearly dependent on incident terahertz wave intensity, making the plasma pressure emission useful as a detector.

Therefore, in single-color laser excitation, the terahertz-wave-enhanced acoustic pressure is quadratically dependent on the terahertz field due to the symmetrical distribution of electron drift velocity. Thus acoustic emission from single-color laser plasma can be used for terahertz wave detection. The advantages of this detection method are: 1) the omnidirectional pattern of the acoustic emission, which enables the signal collection at any direction; 2) the low attenuation of the acoustic wave in the ambient air, which makes it possible to use laser-induced plasma as a sensor to detect terahertz waves at a standoff location while sending information back to the user via acoustic waves. These merits are attractive for remote terahertz sensing; however, one disadvantage of this method is that the detection is incoherent, i.e., no phase information of the terahertz pulse can be recovered from the acoustic signal.

3.2.2 Coherent detection

Compared to the case of single-color laser excitation, the terahertz-wave-enhanced acoustic emission can be quite different if two-color laser fields, E_ω (800 nm) and $E_{2\omega}$ (400 nm), are used for plasma formation. Figure 24 shows the modified experimental layout.

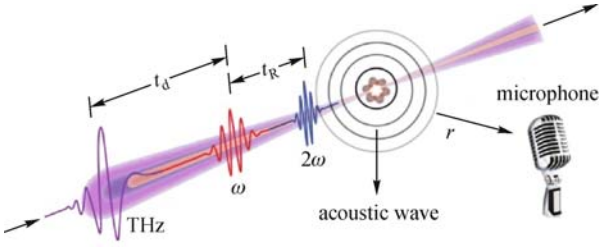

Fig. 24 Experimental schematic for the THz-enhanced acoustics using two-color femtosecond laser excitation

For E_ω and $E_{2\omega}$ laser fields aligned parallel to each other, the combined field $E_{\mathrm{Opt}}(t)$ can be expressed as

$$E_{\mathrm{Opt}}(t) = E_\omega(t) + E_{2\omega}(t) = A_{\omega 0}(t)\cos(\omega t) + A_{2\omega 0}(t)\cos(2\omega t + \phi_{\omega,2\omega}), \quad (7)$$

where $A_{\omega 0}(t)$, $A_{2\omega 0}(t)$ are the envelopes of the E_ω and $E_{2\omega}$ pulses respectively. By changing the relative phase of the two optical fields, $\phi_{\omega,2\omega}$, the drift velocity distribution and electron trajectories can be controlled [51,52].

In order to determine the optical phase dependence on the drift velocity distribution, the terahertz emission from the plasma excited by a two-color laser field is measured at different $\Delta\phi_{\omega,2\omega}$, since the amplitude of terahertz signal is correlated to the asymmetry of the electron drift velocity [53]. The results are shown in Fig. 25 and the zoom of the figure shows the data with sinusoidal fit. We can see that, at the relative phase change $\Delta\phi_{\omega,2\omega}$ of $\pm(2l+1)\pi/2$ (where l is an integer), the electron drift velocity distribution is strongly asymmetric; while at the relative phase change $\Delta\phi_{\omega,2\omega}$ of $\pm l\pi$, the electron drift velocity distribution is almost symmetric. Thereby, information of the electron drift velocity distribution is crucial for coherent control of the acoustic pressure enhancement, and knowledge of electron motion will provide new techniques for coherent terahertz wave detection.

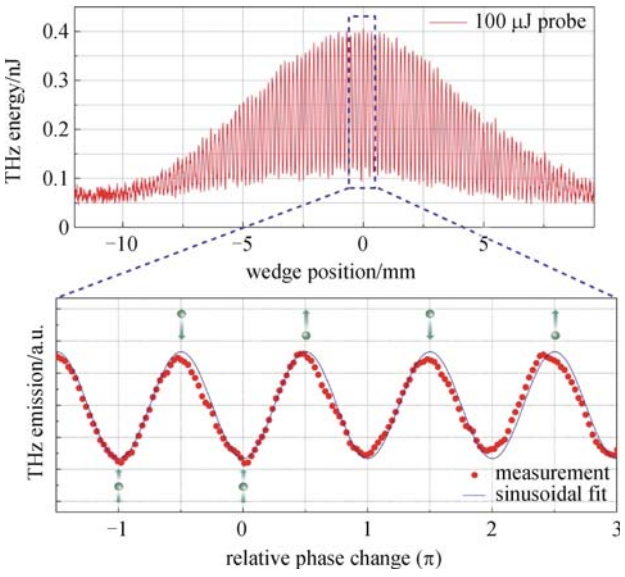

Fig. 25 Dependence of terahertz wave generation from plasma on the relative phase delay between 800 nm pulse and 400 nm pulse. The arrow refers to the electron drift direction. At the maxima of the terahertz emission, the electron drift velocity is highly asymmetric, while at the minima of the terahertz emission, the electron drift velocity is nearly symmetric

While for the excitation of a two-color laser field, the terahertz-wave-induced pressure enhancement $\Delta p(\Delta\phi_{\omega,2\omega})$ takes a more complicated expression including the drift velocity distribution $\rho(\vec{v}(0),\Delta\phi_{\omega,2\omega})$ and initial drift velocity $\vec{v}(0)$ [23]:

$$\Delta p(\Delta\phi_{\omega,2\omega}) \propto n_{\mathrm{e}}\left[\int_{-\infty}^{+\infty}\left(m_{\mathrm{e}}\vec{v}^2(0) + 2m_{\mathrm{e}}\vec{v}(0)\Delta\vec{v}_{\mathrm{e1}}\right)\rho\left(\vec{v}(0),\Delta\phi_{\omega,2\omega}\right)\mathrm{d}\vec{v}(0)/2 + m_{\mathrm{e}}\sum_{i=1}^{\infty}\Delta\vec{v}_{ei}^2\right]. \quad (8)$$

When a terahertz field interacts with a plasma induced by a particular relative optical phase delay between ω and 2ω (affecting the initial electron drift velocity at the time of photoionization), the electrons that experience the terahertz field are either slightly accelerated or decelerated depend-

ing on whether the terahertz field is anti-parallel or parallel to the initial momentum "kick" given to the freed electrons at birth. Scanning the delay between the terahertz and optical pulses "t_d" for relative delays of $-\pi/2$ and $\pi/2$ between the ω and 2ω pulses "t_R", the rising enhancement curves for opposite net electron drift directions are obtained. The results are plotted in Fig. 26(a). In both cases, there is acoustic wave enhancement which results from terahertz-field induced electron heating and increased electron-electron, electron-ion, and electron-molecule collisions; however, under parallel and anti-parallel conditions, the free electrons are either decelerated or accelerated along the direction of the terahertz field, contributing to the overall acoustic emission.

Despite the complex form of Eq. (8), the difference between $\Delta p(-\pi/2)$ and $\Delta p(\pi/2)$ can be reduced to a much more simplified expression by taking the symmetry of $\rho(\vec{v}(0),\pi/2) = \rho(-\vec{v}(0),-\pi/2)$ into consideration. This eliminates the second order term of $\vec{E}_{\mathrm{THz}}2$ while only the first order term $\vec{E}_{\mathrm{THz}}$ is left. Using a mathematical identity and a change of variable, the first two terms of Eq. (8) evaluated at $\pi/2$ can be transformed to

$$-\int_{+\infty}^{-\infty}\left[m_e\left(-v'(0)\right)^2+2m_e\left(-v'(0)\right)\Delta v_{ei}\right]$$

$$\rho\left(-v'(0),\frac{\pi}{2}\right)\frac{\mathrm{d}-v'(0)}{2}, \tag{9}$$

where $v'(0) = -v(0)$. From symmetry, $\rho\left(v(0),\frac{\pi}{2}\right) = \rho\left(-v(0),-\frac{\pi}{2}\right)$ and Eq. (9) can be rewritten as

$$-\int_{-\infty}^{+\infty}\left[m_e\left(-v'(0)\right)^2-2m_e\left(v'(0)\right)\Delta v_{ei}\right]$$

$$\rho\left(v'(0),\frac{\pi}{2}\right)\frac{\mathrm{d}v'(0)}{2}. \tag{10}$$

Changing back to the original variable, Eq. (8) can then be written as

$$-\int_{-\infty}^{+\infty}\left[m_e\left(v(0)\right)^2-2m_e\left(v(0)\right)\Delta v_{ei}\right]\rho\left(v(0),\frac{\pi}{2}\right)\frac{\mathrm{d}v(0)}{2}. \tag{11}$$

Performing the subtraction:

$$\Delta p(-\pi/2)-\Delta p(\pi/2) = 4m_e v(0)\Delta v_{ei}\rho\left(v(0),\frac{\pi}{2}\right)\mathrm{d}v(0)/2. \tag{12}$$

Since $\Delta v_{ei} = -\int_{t_i-\tau}^{t_i} eE_{\mathrm{THz}}(t)\mathrm{d}t/m_e$, by subtracting these two curves, we gain a direct relationship between the terahertz electric field strength and the acoustic pressure enhancement:

$$\Delta p(\pi/2)-\Delta p(-\pi/2) \propto \vec{E}_{\mathrm{THz}}. \tag{13}$$

By subtracting the time resolved acoustic curves for these respective phases, both "background" acoustic emission from the dual color plasma and the second order heating term $E_{\mathrm{THz}}(t)^2$ are cancelled, since these are symmetric for the dual-color ionization, leaving only the change in acoustic emission from electron momentum change by the terahertz field prior to the first collision event, after which the electron drift is randomized and its coherence is lost. In Fig. 26(b), the terahertz waveform obtained by subtracting $\Delta p(-\pi/2)$ from $\Delta p(\pi/2)$ is compared to that obtained by an electro-optic crystal. Figure 26(c) compares the spectra of the respective methods performed in air and the agreement between the well documented water vapor absorption line locations, which give further confidence that acoustic emission can be used to encode spectral information of materials; where the spectral resolution is a function of the scan length. Terahertz-wave-enhanced acoustic emission from two-color laser field-induced plasma therefore offers a unique solution for coherent terahertz wave detection, and has potential for use in remote terahertz wave sensing.

3.3 Remote sensing with acoustics

In addition to initial demonstrations of acoustic spectral encoding at short ranges, the feasibility for carrying these acoustic frequencies over larger distances was investigated. Another broadband microphone, (40AC from GRAS with higher sensitivity at the lower frequency range), was placed at the 3 inch[1)] focus of a 12 inch parabolic collection dish. The entire assembly was moved to varying radial distances from the plasma source. The humidity in the lab during the experiment was approximately 40%. Figure 27 shows higher frequencies are attenuated after 11 meters of propagation (test limited by lab space), but the acoustic pulses contained reasonable bandwidth up to 40 kHz.

This indicates detection of acoustic frequencies well beyond the human limit (20 kHz) is possible at standoff distances. In another experiment, a member of our team stood directly in front of the plasma source and the acoustic signal was collected from several meters. As shown in Fig. 28(a), the acoustic pulse was detected without having a direct line of sight to the plasma. This could be advantageous if information needed to be collected from around a corner or from a separate room that did not allow a direct line of sight to the plasma detector.

Following the acoustic wave propagation experiments, the acoustic modulation induced by the incident terahertz radiation was tested. Due to the particular arrangement of

1) 1 inch $\approx$ 2.54 cm

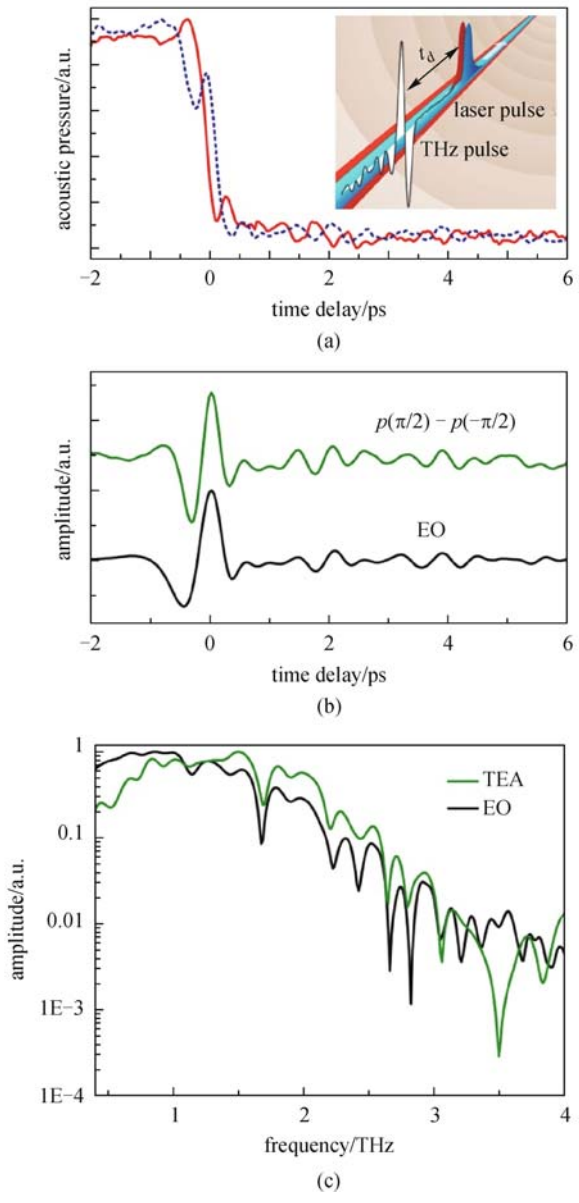

Fig. 26 (a) Acoustic pressure enhancement as a function of time delay t_d at relative phase delay of $\pi/2$ (solid line) and $-\pi/2$ (dashed line). Inset, the experimental schematic of interaction of the terahertz pulse and two-color laser plasma; (b) comparison between the terahertz time-domain waveforms measured by terahertz-wave-enhanced acoustic emission and electro-optic sampling respectively in ambient air; (c) corresponding spectral comparison of the waveforms in (b). TEA; terahertz enhanced acoustics; EO: electro-optic

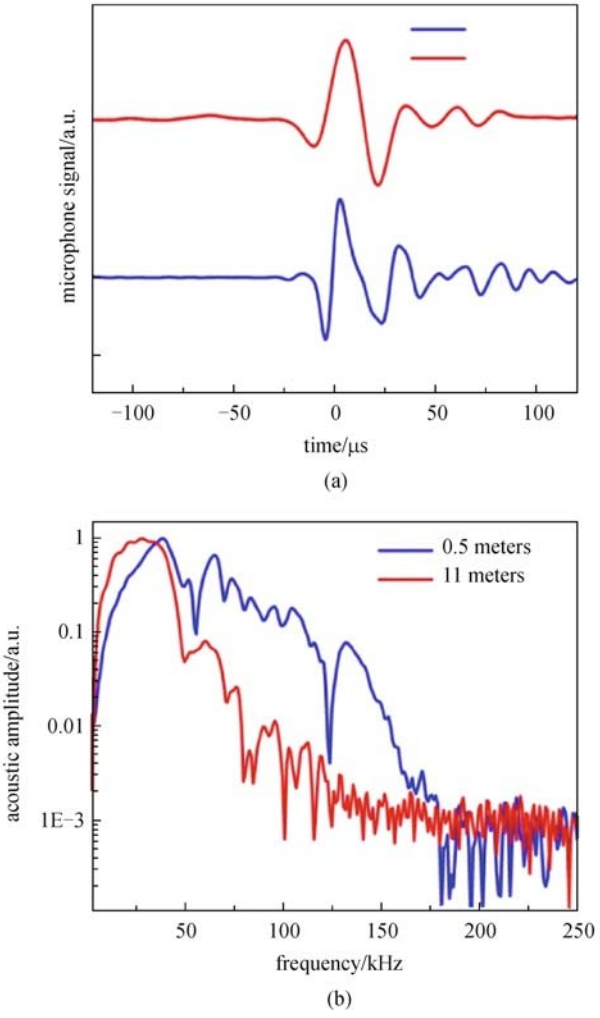

Fig. 27 Temporal and spectral characteristics of acoustic pulses collected using a broadband microphone mounted at the 3 inch focus of a 12 inch diameter parabolic reflector. (a) Normalized temporal pressure transients at 0.5 and 11 meters from the plasma source; (b) normalized spectral comparison of 0.5 and 11 meters acoustic pulse propagation

the experimental setup, the optical pulse energy used to form the acoustic sensor was 100 μJ; an energy only slightly above the ionization threshold needed for plasma formation. At this optical pulse energy level, the plasma is inaudible to the human ear. For this reason, the acoustic signal range was limited to three meters standoff showing 5% modulation, as shown in Fig. 28(b), after 10 averages taken using the 40th harmonic of the laser with a 300 ms time constant.

With an upgrade in the experimental equipment, including higher power optical pulses used for plasma formation, a microphone with higher sensitivities at frequencies, and a larger collection dish used for focusing the acoustic energy onto the microphone, it is expected that the terahertz enhanced acoustic signal could be detected from much greater distances due to large improvements in the system SNR. For example, by using millijoule pulse energies such as those used in Fig. 27, the plasma acoustics are audible from the offices adjacent to the laboratory even with the doors closed.

4 Conclusions

In conclusion, we presented two milestone developments in terahertz wave science and technology geared towards

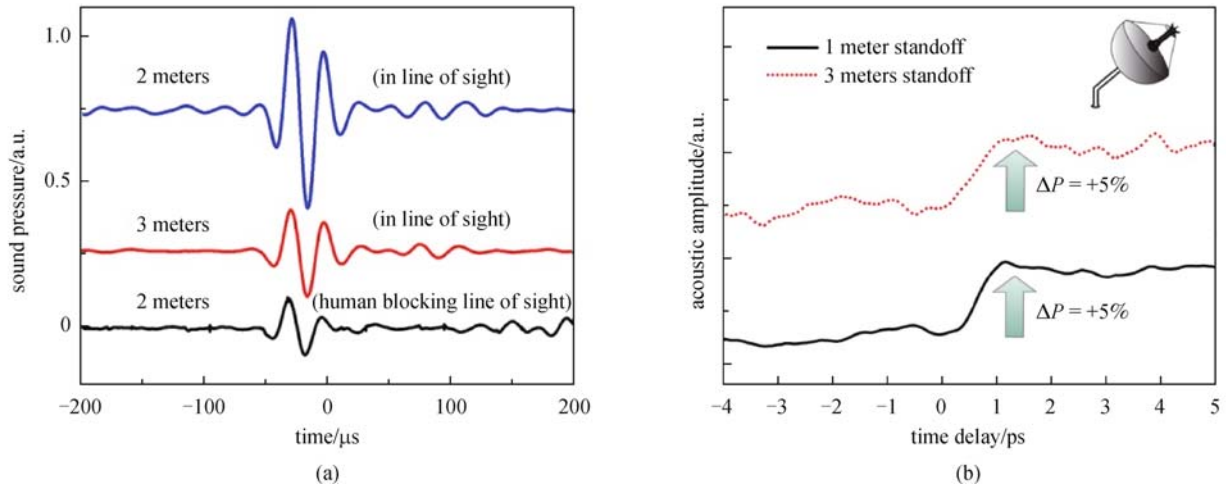

Fig. 28 (a) Acoustic pulses collected with and without direct line of sight to the plasma acoustic source from several meters; (b) terahertz enhanced acoustic signal collected at standoff distance of 1 and 3 meters from the plasma source using a 12" diameter parabolic reflector with the microphone positioned at the 3" focus

coherent detection of terahertz waves using air-based sensors. The photoacoustic and photoluminescent emission, as well as manipulation of electron motion inside a volume of ionized air, were used to overcome existing sensor limitations and extend the useful range of existing terahertz technology. The study will push the development of terahertz field strengths and bandwidths, key applications in spectroscopy, non-invasive evaluation of materials, and imaging.

Acknowledgements This work is supported in part by the Army Research Office-Multidisciplinary University Research Initiative (ARO-MURI), the Defense Threat Reduction Agency (DTRA), National Science Foundation (NSF), and the U.S. Department of Homeland Security through the DHS-ALERT Center under Award 2008-ST-061-ED0001. The views and conclusions contained in this document are those of the authors and should not be interpreted as necessarily representing the official policies, either expressed or implied, of the U.S. Department of Homeland Security.

References

1. Hamster H, Sullivan A, Gordon S, White W, Falcone R W. Subpicosecond, electromagnetic pulses from intense laser-plasma interaction. Physical Review Letters, 1993, 71(17): 2725–2728
2. Cook D J, Hochstrasser R M. Intense terahertz pulses by four-wave rectification in air. Optics Letters, 2000, 25(16): 1210–1212
3. Bartel T, Gaal P, Reimann K, Woerner M, Elsaesser T. Generation of single-cycle THz transients with high electric-field amplitudes. Optics Letters, 2005, 30(20): 2805–2807
4. Xie X, Dai J M, Zhang X C. Coherent control of THz wave generation in ambient air. Physical Review Letters, 2006, 96(7): 075005-1–075005-4
5. Dai J M, Xie X, Zhang X C. Detection of broadband terahertz waves with a laser-induced plasma in gases. Physical Review Letters, 2006, 97(10): 103903-1–103903-4
6. Lu X F, Karpowicz N, Chen Y Q, Zhang X C. Systematic study of broadband terahertz gas sensor. Applied Physics Letters, 2008, 93 (26): 261106-1–261106-3
7. Ho I C, Guo X Y, Zhang X C. Design and performance of reflective terahertz air-biased-coherent-detection for time-domain spectroscopy. Optics Express, 2010, 18(3): 2872–2883
8. Kim K Y, Glownia J H, Taylor A J, Rodriguez G. Terahertz emission from ultrafast ionizing air in symmetry-broken laser fields. Optics Express, 2007, 15(8): 4577–4584
9. Karpowicz N, Zhang X C. Coherent terahertz echo of tunnel ionization in gases. Physical Review Letters, 2009, 102(9): 093001-1–093001-4
10. Wu H C, Meyer-ter-Vehn J, Sheng Z M. Phase-sensitive terahertz emission from gas targets irradiated by few-cycle laser pulses. New Journal of Physics, 2008, 10(4): 043001-1–043001-10
11. Silaev A A, Vvedenskii N V. Quantum-mechanical approach for calculating the residual quasi-dc current in a plasma produced by a few-cycle laser pulse. Physica Scripta, 2009, T135: 014024-1–014024-5
12. Karpowicz N, Dai J, Lu X, Chen Y, Yamaguchi M, Zhao H, Zhang X C, Zhang L, Zhang C, Price-Gallagher M, Fletcher C, Mamer O, Lesimple A, Johnson K. Coherent heterodyne time-domain spectrometry covering the entire “terahertz gap”. Applied Physics Letters, 2008, 92(1): 011131-1–011131-3
13. Xu J, Zhang X C. Introduction to THz Wave Photonics, New York: Springer, 2010
14. Wu Q, Zhang X C. Free space electro optic sampling of terahertz beams. Applied Physics Letters, 1995, 67(24): 3523–3525
15. Jepsen P U, Winnewisser C, Schall M, Schyja V, Keiding S R, Helm

H. Detection of THz pulses by phase retardation in lithium tantalite. Physical Review E: Statistical Physics, Plasmas, Fluids, and Related Interdisciplinary Topics, 1996, 53(4): R3052–R3054
16. Nahata A, Auston D, Heinz T, Wu C. Coherent detection of freely propagating terahertz radiation by electro optic sampling. Applied Physics Letters, 1996, 68(2): 150–152
17. Thomson M D, Blank V, Roskos H G. Terahertz white-light pulses from an air plasma photo-induced by incommensurate two-color optical fields. Optics Express, 2010, 18(22): 23173–23182
18. Nahata A, Heinz T F. Detection of freely propagating terahertz radiation by use of optical second-harmonic generation. Optics Letters, 1998, 23(1): 67–69
19. Cook D, Chen J, Morlino E, Hochstrasser R. Terahertz-field-induced second-harmonic generation measurements of liquid dynamics. Chemical Physics Letters, 1999, 309(3–4): 221–228
20. Shelton D P. Nonlinear-optical susceptibilities of gases measured at 1064 and 1319 nm. Physical Review A, 1990, 42(5): 2578–2592
21. Newport Corporation. Newport Announces Terahertz Pulse Generation Kit. 2012, http://www.openpr.com/news/180698/Newport-Announces-Terahertz-Pulse-Generation-Kit.html
22. Zomega Terahertz Corporation. 2012, http://www.z-thz.com/
23. Liu J L, Zhang X C. Terahertz-radiation-enhanced emission of fluorescence from gas plasma. Physical Review Letters, 2009, 103 (23): 235002-1–235002-4
24. Liu J L, Zhang X C. Enhancement of laser-induced fluorescence by intense terahertz pulses in gases. IEEE Journal on Selected Topics in Quantum Electronics, 2011, 17(1): 229–236
25. Liu J L, Dai J M, Chin S L, Zhang X C. Broadband terahertz wave remote sensing using coherent manipulation of fluorescence from asymmetrically ionized gases. Nature Photonics, 2010, 4(9): 627–631
26. Davies A G, Burnett A D, Fan W, Linfield E H, Cunningham J E. Terahertz spectroscopy of explosives and drugs. Materials Today, 2008, 11(3): 18–26
27. Ferguson B, Zhang X C. Materials for terahertz science and technology. Nature Materials, 2002, 1(1): 26–33
28. Ho L, Pepper M, Taday P. Terahertz spectroscopy: signatures and fingerprints. Nature Photonics, 2008, 2(9): 541–543
29. Hebling J, Yeh K L, Hoffmann M C, Bartal B, Nelson K A. Generation of high-power terahertz pulses by tilted-pulse-front excitation and their application possibilities. Journal of the Optical Society of America B, Optical Physics, 2008, 25(7): B6–B19
30. Wanke M C, Mangan M A, Foltynowicz R J. Atmospheric Propagation of THz Radiation. Technical Report SAND2005-6389. Albuquerque: Sandia National Laboratories, 2005
31. Dai J M, Zhang X C. Demonstration of 17 meter standoff THz wave generation. In: Proceedings of Nonlinear Optics: Materials, Fundamentals and Applications. Optical Society of America, 2009, NWA1
32. Dai J M, Zhang X C. Terahertz wave generation from gas plasma using a phase compensator with attosecond phase-control accuracy. Applied Physics Letters, 2009, 94(2): 021117-1–021117-3
33. Wang T J, Yuan S, Chen Y P, Daigle J F, Marceau C, Théberge F, Châteauneuf M, Dubois J, Chin S L. Toward remote high energy terahertz generation. Applied Physics Letters, 2010, 97(11): 111108-1–111108-3
34. Clough B, Liu J L, Zhang X C. Laser-induced photoacoustics influenced by single-cycle terahertz radiation. Optics Letters, 2010, 35(21): 3544–3546
35. Liu J L, Clough B, Zhang X C. Enhancement of photoacoustic emission through terahertz-field-driven electron motions. Physical Review E: Statistical, Nonlinear, and Soft Matter Physics, 2010, 82 (6): 066602-1–066602-6
36. Roskos H G, Thomson M D, Kreß M, Löffler T. Broadband THz emission from gas plasmas induced by femtosecond optical pulses: From fundamentals to applications. Laser & Photonics Reviews, 2007, 1(4): 349–368
37. Chen J, Chen Y Q, Zhao H W, Bastiaans G J, Zhang X C. Absorption coefficients of selected explosives and related compounds in the range of 0.1 – 2.8 THz. Optics Express, 2007, 15(19): 12060–12067
38. Liu H B, Zhong H, Karpowicz N, Chen Y Q, Zhang X C. Terahertz spectroscopy and imaging for defense and security applications. Proceedings of the IEEE, 2007, 95(8): 1514–1527
39. Filin A, Compton R, Romanov D A, Levis R J. Impact-ionization cooling in laser-induced plasma filaments. Physical Review Letters, 2009, 102(15): 155004-1–155004-4
40. Radziemski L J, Loree T R, Cremers D A, Hoffman N M. Time-resolved laser-induced breakdown spectrometry of aerosols. Analytical Chemistry, 1983, 55(8): 1246–1252
41. Sobral H, Villagran-Muniz M, Navarro-Gonzalez R, Raga A C. Temporal evolution of the shock wave and hot core air in laser induced plasma. Applied Physics Letters, 2000, 77(20): 3158–3160
42. Raizer Y P. Laser-Induced Discharge Phenomena. New York: Consultants Bureau, 1977
43. Diebold G J. Topics in Current Physics. Heidelberg: Springer-Verlag, 1989
44. Fay R D. Plane sound waves of finite amplitude. Journal of the Acoustical Society of America, 1931, 3(2A): 222–241
45. Hamilton M, Blackstock D. Nonlinear Acoustics. San Diego: Academic Press, 1997
46. Mlejnek M, Wright E M, Moloney J V. Femtosecond pulse propagation in argon: A pressure dependence study. Physical Review E: Statistical Physics, Plasmas, Fluids, and Related Interdisciplinary Topics, 1998, 58(4): 4903–4910
47. Tzortzakis S, Prade B, Franco M, Mysyrowicz A. Time-evolution of the plasma channel at the trail of a self-guided IR femtosecond laser pulse in air. Optics Communications, 2000, 181(1–3): 123–127
48. Gibson G N, Freeman R R, McIlrath T J. Dynamics of the high-intensity multiphoton ionization of N_2. Physical Review Letters, 1991, 67(10): 1230–1233
49. Yu J, Mondelain D, Kasparian J, Salmon E, Geffroy S, Favre C, Boutou V, Wolf J P. Sonographic probing of laser filaments in air. Applied Optics, 2003, 42(36): 7117–7120
50. Ni X W, Zou B, Chen J P, Biao B M, Shen Z H, Lu J, Cui Y P. On the generation of laser-induced plasma acoustic waves. Acta Physica

Sinica, 1998, 7(2): 143–147
51. Kim K Y, Glownia J H, Taylor A J, Rodriguez G. Terahertz emission from ultrafast ionizing air in symmetry-broken laser fields. Optics Express, 2007, 15(8): 4577–4584
52. Dai J, Karpowicz N, Zhang X C. Coherent polarization control of terahertz waves generated from two-color laser-induced gas plasma. Physical Review Letters, 2009, 103(2): 023001-1–023001-4
53. Kim K Y, Taylor A J, Glownia J H, Rodriguez G. Coherent control of terahertz supercontinuum generation in ultrafast laser-gas interactions. Nature Photonics, 2008, 2(10): 605–609

Benjamin Clough–graduated from the University of New Mexico with a B.S. degree in Electrical Engineering in Dec. 2006. He received his Ph.D degree in Electrical, Computer, and Systems Engineering in May of 2012 from Rensselaer Polytechnic Institute, Troy NY. He is the author or coauthor of more than 8 journal publications, 16 conference publications and presentations, 1 US patent disclosure, and a contributor to 2 book chapters. He has been involved in a variety of interdisciplinary projects including electronics design, embedded control, ultrafast optics, software development, and terahertz science and technology. He has over 10 years of combined laboratory experience and has worked in several different environments including Sandia National Labs, Honeywell, Rensselaer, and now the Department of Defense. He was awarded the RPI Founder's Award of Excellence and the NSF IGERT Fellowship in 2009, the DOD SMART scholarship in 2011, and was the winner of the $30000 Lemelson-MIT Student Prize in 2011 for his research developing alternative methods for terahertz detection using laser plasma-induced acoustic waves. He currently works for the Department of Defense, where he provides subject matter expertise and manages technical programs developing technology to counter improvised explosive devices.

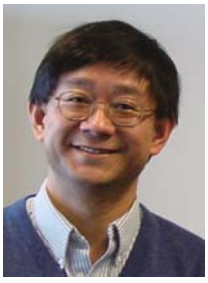

Xi-Cheng Zhang–Parker Givens Chair of Optics, assumes Directorship of The Institute of Optics, University of Rochester (UR), NY, a foremost institution in optics and optical physics research and education, on 1/1/2012. Prior to joining UR, he pioneered world-leading research in the field of ultrafast laser-based terahertz technology and optical physics at Rensselaer Polytechnic Institute (RPI), Troy NY (1992–2012). At RPI, he is the Eric Jonsson Professor of Science; Acting Head at the Department of Physics, Applied Physics & Astronomy; Professor of Electrical, Computer & System; and Founding Director of the Center for THz Research. He is co-founder of Zomega Terahertz Corp. With a B.S. (1982) from Peking University, he earned the M.S. (1983) and Ph.D. degree (1985) in Physics from Brown University, RI.

Previous positions included Visiting Scientist at MIT (1985), Physical Tech. Division of Amoco Research Center (1987), EE Dept. at Columbia University (1987–1991); Distinguished Visiting Scientist at Jet Propulsion Lab, Caltech (2006). He holds 27 U.S. patents, and is a prolific author and speaker. He is a Fellow of AAAS, APS (lifetime), IEEE, OSA (lifetime), and SPIE (lifetime). Dr. Zhang is serving as Editor-in-Chief of Optics Letters (2014 – 2016).

His honors and awards include: IRMMW-THz Kenneth Button Prize (2014); OSA William F. Meggers Award (2012); IEEE Photonics Society William Streifer Scientific Achievement Award (2011); Rensselaer William H. Wiley 1866 Award (2009); Japan Society for the Promotion of Science Fellowship & NRC-CIAR Distinguished Visiting Scientist, Ottawa, Canada (2004); and First Heinrich Rudolf Hertz Lecturer, RWTH, Aachen, Germany (2003). He also served two years as a Distinguished Lecturer of IEEE/LEOS. He received Rensselaer Early Career Award (1996), Research Corporation Cottrell Scholar Award (1995), NSF Early Career Award (1995), K. C. Wong Prize, K. C. Wong Foundation, Hong Kong (1995), NSF Research Initiation Award (1992). In 1993 – 1994, he was an AFOSR-SRPF Fellow at Hanscom Air Force Base.